Solid Earth

Open Access

EGU

Structural characterization and K–Ar illite dating of reactivated, complex and heterogeneous fault zones: lessons from the Zuccale Fault, Northern Apennines

Giulio Viola[1]**, Giovanni Musumeci**[2,3]**, Francesco Mazzarini**[3]**, Lorenzo Tavazzani**[4]**, Manuel Curzi**[1]**, Espen Torgersen**[5]**, Roelant van der Lelij**[5]**, and Luca Aldega**[6]

[1]Dipartimento di Scienze Biologiche, Geologiche ed Ambientali - BiGeA, Università di Bologna, Bologna, Italy
[2]Dipartimento di Scienze della Terra, Università di Pisa, Pisa, Italy
[3]Istituto Nazionale di Geofisica e Vulcanologia, Pisa, Italy
[4]Institute of Geochemistry and Petrology, ETH Zürich, 8092 Zürich, Switzerland
[5]Geological Survey of Norway, Trondheim, Norway
[6]Dipartimento di Scienze della Terra, Sapienza Università di Roma, Rome, Italy

Correspondence: Giulio Viola (giulio.viola3@unibo.it)

Abstract. We studied the Zuccale Fault (ZF) on Elba, part of the Northern Apennines, to unravel the complex deformation history that is responsible for the remarkable architectural complexity of the fault. The ZF is characterized by a patchwork of at least six distinct, now tightly juxtaposed brittle structural facies (BSF), i.e. volumes of deformed rock characterized by a given fault rock type, texture, colour, composition, and age of formation. ZF fault rocks vary from massive cataclasite to foliated ultracataclasite, from clay-rich gouge to highly sheared talc phyllonite. Understanding the current spatial juxtaposition of these BSFs requires tight constraints on their age of formation during the ZF lifespan to integrate current fault geometries and characteristics over the time dimension of faulting. We present new K–Ar gouge dates obtained from three samples from two different BSFs. Two top-to-the-east foliated gouge and talc phyllonite samples document faulting in the Aquitanian (ca. 22 Ma), constraining east-vergent shearing along the ZF already in the earliest Miocene. A third sample constrains later faulting along the exclusively brittle, flat-lying principal slip surface to < ca. 5 Ma. The new structural and geochronological results reveal an unexpectedly long faulting history spanning a ca. 20 Myr time interval in the framework of the evolution of the Northern Apennines. The current fault architecture is highly heterogeneous as it formed at very

different times under different conditions during this prolonged history. We propose that the ZF started as an Aquitanian thrust that then became selectively reactivated by early Pliocene out-of-sequence thrusting during the progressive structuring of the Northern Apennine wedge. These results require the critical analysis of existing geodynamic models and call for alternative scenarios of continuous convergence between the late Oligocene and the early Pliocene with a major intervening phase of extension in the middle Miocene allowing for the isostatic re-equilibration of the Northern Apennine wedge. Extension started again in the Pliocene and is still active in the innermost portion of the Northern Apennines. In general terms, long-lived, mature faults can be very architecturally complex. Their unravelling, including understanding the dynamic evolution of their mechanical properties, requires a multidisciplinary approach combining detailed structural analyses with dating the deformation events recorded by the complex internal architecture, which is a phenomenal archive of faulting and faulting conditions through time and space.

1 Introduction and aims of the study

Faults control fluid migration and storage and mineralizations, which makes them of great significance to society. In addition, although faults only occupy a small volume of the crust, they control its modes of deformation by localizing coseismic slip or aseismic creep, thus being sources of seismic hazard that deserve attention from the scientific community. After initial localization, progressive fault growth leads to relatively narrow fault cores, where slip is mostly accommodated, and surrounding fractured damage zones. Different fault rocks (e.g. cataclasite, gouge, pseudotachylyte, phyllonite, and mylonite, each representative of specific faulting conditions; e.g. Sibson, 1977; Wise et al., 1984) may form at different stages of the faulting history of the same fault. This implies that the spatial relationships among different fault rocks in the same fault may be difficult to untangle, as multiple fault rock domains are commonly intricately juxtaposed to form complex fault architectures. Indeed, faults are rarely simple discrete and tabular slip surfaces. Instead, they commonly exhibit significant along- and across-strike architectural variations due to fault propagation and linkage processes in space and time, different physical and chemical conditions during fluid–rock interaction, and the ease of reactivation over time of brittle structures at different depths. Existing conceptual models of fault zones (e.g. Caine et al., 1996; Wibberley and Shimamoto, 2003), their accuracy notwithstanding, seldomly consider the absolute timing of faulting and are generally rather static snapshots of long-lasting, cumulative evolutions. In turn, this may lead to oversimplifications and misinterpretations of the role of faults, their hydraulic properties and mechanics, and ultimately their seismic behaviour. In addition, such a partially incomplete representation of the true nature of faults may also lead to erroneous or biased tectonic reconstructions. Unravelling the internal structure of faults, while integrating it over their entire lifetime span is therefore paramount to understanding the full spectrum of mechanical, hydraulic, and seismological behaviours of the crust and accurately reconstructing deformation and tectonic histories. Within regional-scale fault systems, repeated faulting events cause deformation to progressively localize into mechanically weaker rock volumes and along discrete slip surfaces. Variably deformed structural domains or lithons can be preserved within fault cores, and they represent "archives" of the inherited geometric, kinematic, mechanic, geochemical, and isotopic signatures of faulting. These domains have recently been explicitly referred to as "brittle structural facies – BSF" by Tartaglia et al. (2020), who further elaborated on the concept of "fault facies" that is at times used in the context of hydrocarbon reservoirs (e.g. Braathen et al., 2009). In more detail, Tartaglia et al. (2020) use the term BSF to specifically refer "to a deformed volume of rock characterized by a given fault rock type, texture, colour, composition, and age of formation" (e.g. their Fig. 7). Field studies do lend support to this approach and show that BSFs generally exhibit sharp boundaries and complex crosscutting relationships, and their identification, characterization, and spatial and temporal sorting requires detailed structural analyses (e.g. Wang et al., 2016; Scheiber et al., 2019; Vignaroli et al., 2020). This is because, even though different BSFs may currently be found side by side in a fault core and/or damage zone, they possibly formed at very different geological times and environmental or structural conditions. Their study is therefore necessary to establish the relative temporal sequence of fault initiation and their mechanical evolution. In this framework, the current physical juxtaposition of BSFs as a constituent element of a fault architecture is due to the temporal and spatial evolution of the fault, such that many brittle faults are best interpreted as the summation of multiple deformation episodes.

To improve our understanding of faulting and produce time-constrained models firmly based on physical and chemical constraints, a deep knowledge of the structural, mechanical, hydrogeological, and petrophysical properties of BSFs is required and geologists need to pay particular attention to their characterization when unravelling the deformation history preserved in the rock record of fault zones.

To contribute to this issue and further develop our understanding of fault zones and faulting, we document here how conclusions based on the study of fault rocks that are presently tightly juxtaposed in an architecturally complex fault may potentially be misleading or may be revealing only part of long and complex geological histories unless they are based upon the direct dating of all or some of the juxtaposed BSFs. We use the Zuccale Fault (from now on referred to as ZF) on Elba in the northern Apennines of Italy as an example of a multiply reactivated complex fault. Structural characterization of its constituent BSFs and their direct dating by illite K–Ar geochronology allows us to constrain a geological history that is remarkably longer than previously assumed, and the unravelling of this history suggests deformation in the inner portion of the Northern Apennines to be more articulated than generally reported. Lastly, we discuss the potential implications of our new results on the tectonic history of the Northern Apennines orogenic wedge from the early Miocene to the early Pliocene.

2 Methods

Our study relies on an integrated approach combining the multiscalar structural analysis and characterization of the ZF according to classic field and petrographic approaches and the K–Ar dating of selected, representative fault rocks. These were sampled from well-characterized BSFs of the ZF. The dated material was additionally qualitatively and quantitatively characterized by X-ray diffraction (XRD) analysis and transmission electron microscope (TEM) imaging of selected grain size fractions to characterize the finest dated mineral phases.

The analytical procedures for separating, characterizing, and dating the samples are described in detail in Viola et al. (2018) and represent the workflow at the laboratory for clay characterization and K–Ar dating at the Geological Survey of Norway. Fault rocks were disintegrated using approximately 100 freeze–thaw cycles, and clays were suspended in deionized water. Sedimentation with Stokes law and a combination of continuous flow and fixed-angle rotor centrifuges were used to generate particle sizes of < 0.1, 0.1–0.4, 0.4–2, 2–6, and 6–10 µm. Argon was extracted from clay aliquots packed in Mo foil in a stainless steel ultra-high vacuum line using a Pond Engineering furnace at 1400 °C. The evolved sample gas was purified in a first stage using a titanium sublimation pump and in a second stage with one SAES GP50 getter at room temperature and one SAES GP50 getter at 350 °C. Sample gas was spiked with approximately 2×10^{-13} mol of pure ^{38}Ar (Schumacher, 1975) and analysed in an IsotopX NGX multicollector noble gas mass spectrometer fitted with five Faraday cups for 600 integrations of 1 s each. Nominal argon beam intensities were determined by using a second-degree polynomial regression to gas inlet time zero with an in-house Python program. Beam intensities for ^{38}Ar and ^{36}Ar were corrected for mass discrimination relative to ^{40}Ar by a power law (e.g. Renne et al., 2009), using the weighted mean ^{40}Ar / ^{36}Ar ratios of 299.781 ± 0.014 measured from atmospheric argon in an online air pipette and the atmospheric argon composition of Lee et al. (2006). Radiogenic ^{40}Ar* concentrations and their uncertainties were calculated using the equations outlined in Hałas and Wójtowicz (2014). Within this analytical batch, four aliquots of GA-1550 biotite (98.5 ± 0.5 Ma; Mcdougall and Wellman, 2011) were analysed and yielded a weighted mean age of 98.53 ± 0.36 Ma. Potassium concentrations were determined by fusing an aliquot of approximately 50 mg in lithium tetraborate at ~ 1000 °C to form a glass, which was then dissolved in HNO_3 with a rhodium internal standard at 5 ppm prior to analysis with a Perkin Elmer Optima 4300 DV inductively coupled plasma optical emission spectrometer (ICP-OES). K–Ar dates were calculated using the ^{40}K abundance and decay constants of Steiger and Jäger (1977).

XRD analyses were carried out at the Academic Laboratory of Basin Analysis (ALBA) of Roma Tre University (Italy) with a Scintag X1 X-ray system (CuKα radiation). The tube current and the voltage were 30 mA and 40 kV, respectively. Randomly oriented whole-rock powders of all subfractions were X-rayed with a step size of $0.05°$ 2θ and a counting time of 3 s per step in the 2–70° 2θ range. Standard patterns for illite $1M_d$ and $2M_1$ polytypes were represented by the pure illites PDU and SG4 (Eberl et al., 1987), respectively. Integrated peak areas of minerals and illite polytype reflections were transformed into mineral concentration by using mineral intensity factors as a calibration constant (for a review, see Moore and Reynolds, 1997). The estimated quantification error is ± 5 %.

TEM imaging and energy dispersive spectroscopy analysis were performed at the NORTEM infrastructure at the TEM Gemini Centre of the Norwegian University of Science and Technology (NTNU) in Trondheim, Norway. Samples were dispersed at a concentration of 10 ppm by weight in deionized water and dried on a carbon-supported TEM grid. Images were obtained on a JEOL JEM-2100 TEM with a LaB6 filament and chemical information was collected using an Oxford X-Max 80 silicon drift detector (SDD) energy dispersive X-ray analyser (EDX).

3 Geological introduction

The Northern Apennines (Fig. 1) form a stack of northeast- to east-vergent thrust sheets scraped off from the oceanic and continental lithosphere during the Upper Cretaceous–Eocene convergence between the European and the Adriatic plates. Convergence caused the closure of the intervening Piedmont–Liguria Ocean Ocean and subsequent Miocene continental collision (Boccaletti et al., 1971; Carmignani et al., 2001).

Located in the northern Tyrrhenian Sea, Elba belongs to the Northern Apennines inner sector and consists of five metamorphic and non-metamorphic tectonic units derived from both the (i) Adria continental (e.g. Tuscan Nappe) and (ii) Ligurian oceanic domain (e.g. Ligurian Unit), stacked with a general transport direction toward the northeast during orogenic shortening (Boccaletti et al., 1971; Keller and Coward, 1996; Bortolotti et al., 2001).

The tectonic units within this nappe stack are organized into two major thrust complexes (Musumeci and Vaselli, 2012; Massa et al., 2017; Papeschi et al., 2021). The Upper Complex is an imbricate fan formed of three thrust sheets of sedimentary and low-grade metamorphic rocks ascribable to the Ligurian Units and the Tuscan Nappe. The Lower Complex instead consists of two metamorphic units, namely the Calamita Unit overlain by the Ortano Unit, both derived from the Adriatic continental domain (Fig. 1a).

The Upper Complex and Lower Complex are juxtaposed along a major N–S-striking and W-dipping thrust fault, the Capo Norsi–Monte Arco thrust (CN–MAT of Viola et al., 2018; Musumeci and Vaselli, 2012), which is outlined by an intensely deformed slice of Ligurian serpentinized peridotites sandwiched between the metamorphic Ortano Unit below and the overlying Tuscan Nappe sedimentary sequence. As a whole, the system forms a W-dipping, 10 km wide, and 15 km long monocline that defines the first-order geological structure of eastern and central Elba (Barberi et al., 1967; Pertusati et al., 1993; Keller and Coward, 1996; Bortolotti et al., 2001; Papeschi et al., 2021; Ryan et al., 2021).

The nappe stack hosts two large monzogranitic intrusions (Monte Capanne and Porto Azzurro plutons) and a laccolith system that emplaced at shallow depths (5 to 7 km) between
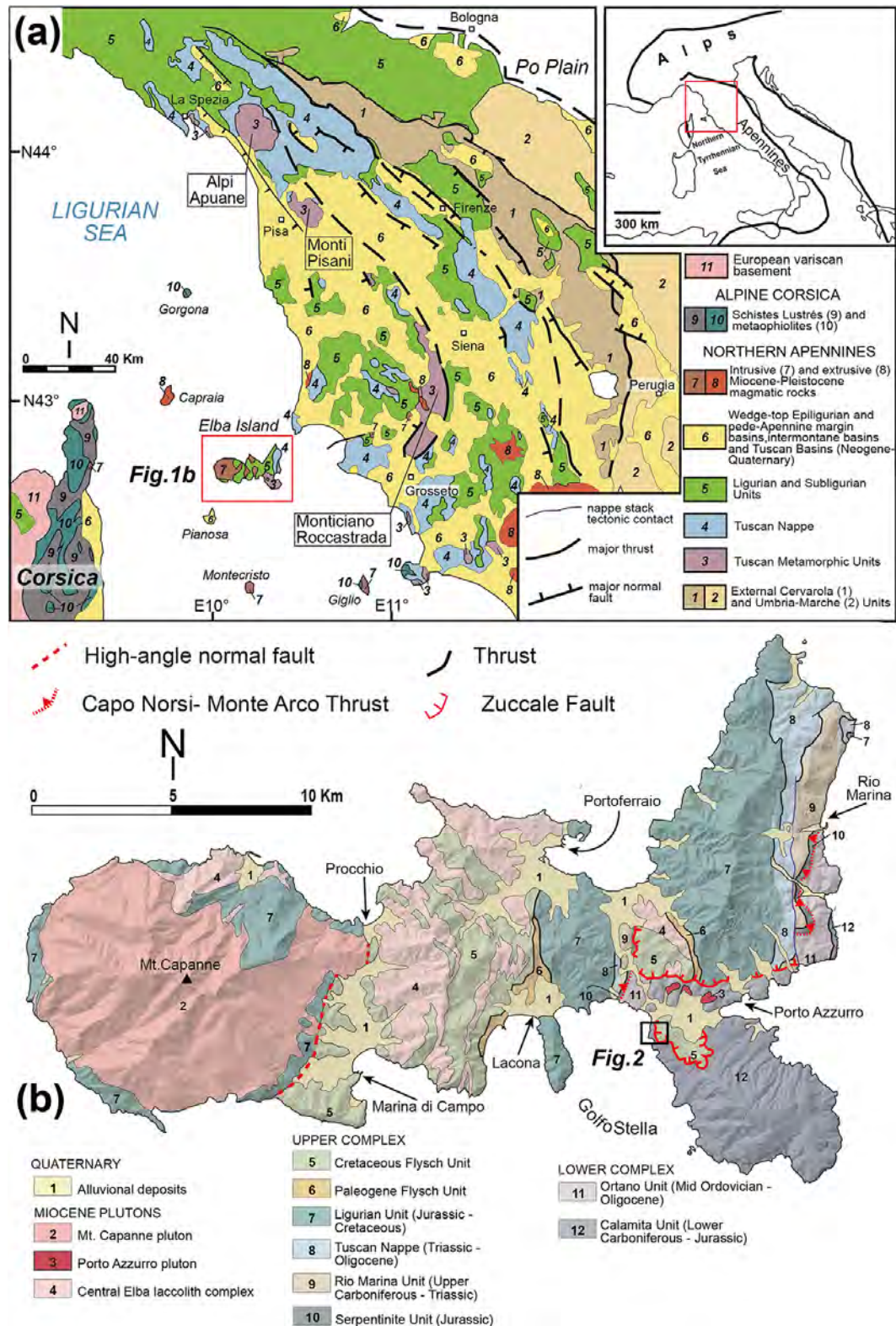
Figure 1. (a) Geological sketch map of the Northern Apennines. Elba is framed by the red box and shown in detail in **(b)**. **(b)** Simplified geological map of Elba. The black square indicates the position of Punta Zuccale, the geology of which is shown in Fig. 2. Modified after Viola et al. (2018).

ca. 8 and 5.9 Ma (Dini et al., 2002; Barboni et al., 2015). Specific to the Porto Azzurro pluton (which is of direct interest to this study), the estimated pressure–temperature (P–T) conditions associated with its contact aureole are reported as characterized by $P_{max} < 0.18$–0.2 GPa and T ranging from 300 °C (biotite zone) to 650 °C (andalusite–K-feldspar zone and wollastonite zone; Duranti et al., 1992; Caggianelli et al., 2018; Papeschi et al., 2019). These P–T conditions are diagnostic of low-pressure and high-temperature (LP–HT) contact metamorphism and indicate that the Porto Azzurro pluton was emplaced at a very shallow crustal level. The emplacement-related thermal anomaly caused diffuse, late Miocene LP–HT metamorphism with amphibolite facies mineral assemblages that are the main metamorphic record in the Calamita and Ortano units (Duranti et al., 1992; Musumeci and Vaselli, 2012; Papeschi et al., 2017; Papeschi and Musumeci, 2019). Early Miocene blueschist facies metamorphism (Bianco et al., 2015; Papeschi et al., 2020 and reference therein) related to the late Oligocene–early Miocene Apennine subduction (Ryan et al., 2021) is only preserved in the northernmost Ortano unit, which escaped the thermal overprint.

According to existing reconstructions, the tectonic evolution of the nappe stack in the easternmost part of Elba is interpreted as resulting from late Oligocene–early Miocene SW–NE shortening, which caused folding and nappe stacking. Compression was followed by middle to late Miocene extension broadly coeval with magmatism and the formation of sedimentary basins in the mainland immediately to the east of Elba and related to either fundamental geodynamic processes causing the opening of the northern Tyrrhenian Sea (e.g. Keller and Coward, 1996) and/or more local factors associated with magma emplacement and ballooning (Pertusati et al., 1993; Bortolotti et al., 2001; Westerman et al., 2004).

Recently, however, mapping and structural observations aided by geochronology have led some authors to a partial reinterpretation of the nappe stack tectonic evolution that can be summarized by the following four evolutionary stages.

i. The first stage is Oligocene to early Miocene folding and nappe stacking under very low metamorphic grade conditions (i.e. anchizone) in the Upper Complex and greenschist to blueschist metamorphism in the Lower Complex. The early Miocene blueschist facies metamorphism is recorded and well preserved in the northernmost Acquadolce Subunit of the Ortano Unit (Bianco et al., 2015; Papeschi et al., 2020, 2021; Ryan et al., 2021);

ii. The second stage represents a middle Miocene extension of the stack upper portion due to the gravitational readjustment of the orogenic wedge causing the tectonic elision of part of the Tuscan Nappe (Decandia et al., 1993; Massa et al., 2017).

iii. The third stage corresponds to middle to late Miocene folding and out-of-sequence thrusting that reshaped the nappe stack (Musumeci and Vaselli, 2012; Papeschi et al., 2017; Viola et al., 2018; Papeschi et al., 2021). The slice of Ligurian peridotites tectonically sandwiched between the Upper Complex and Lower Complex along the CN–MAT supports out-of-sequence thrusting associated with the formation of east-facing thrust anticlines (e.g. Massa et al., 2017). The geochronology of Neogene illite in fault gouge from the CN–MAT constrains this pulse of renewed shortening to ca. 5 Ma (Viola et al., 2018), which is distinctly younger than the emplacement of the Miocene Porto Azzurro pluton dated to between 7 and 6 Ma (Gagnevin et al., 2011; Musumeci et al., 2015).

iv. The fourth stage represents a renewed extension associated with the present-day extensional seismotectonic features of the entire inner part of the Northern Apennines (e.g. Faccenna et al., 2014).

In summary, recent mapping and structural data integrated by K–Ar geochronology of synkinematic illite from key fault gouge samples argue for a complex tectonic evolution wherein shortening pulses have continued to the early Pliocene, with a discrete, significant phase of extension in the middle Miocene (Viola et al., 2018). In this different scenario, the ZF (see below) has also been recently reinterpreted as having partly accommodated one late increment of out-of-sequence thrusting on the Elba (Musumeci et al., 2015; Viola et al., 2018).

4 The Zuccale Fault

The ZF (Fig. 2) was first described and interpreted as a low-angle detachment fault (LANF) that cuts the central–eastern Elba nappe stack down-section with a top-to-the-east displacement of ca. 6 km (Keller and Pialli, 1990; Keller and Coward, 1996). Its first-order main structural domains are as follows.

– First, there is a purely brittle fault zone composed of breccia, cataclasite, and gouge forming a 3 to 5 m thick heterogeneous fault core.

– Second, a generally east-dipping low-angle ($< 5°$) discrete principal slip surface (PSS) is found, where pervasive subhorizontal slickenlines and crystal fibre lineations and associated asymmetric structures are consistent with dominant top-to-the-east–northeast slip.

– Third, there is an up to 3 m thick foliated domain comprising (1) a W- to NW-dipping foliation defined by the preferred orientation of phyllosilicates in clay-rich gouge, (2) subhorizontal shear planes at the contact between gouge and intact host rock, and (3) E- to SE-dipping Riedel shears.

Following the initial description of this remarkable fault structure and the structural characterization of the above-mentioned domains and features, over the last decade numerous studies have dealt with the ZF mechanic and dynamic significance and with its kinematic relevance within the framework of the overall evolution of the Northern Apennines orogenic wedge. Collettini and Holdsworth (2004), for example, first reported a spatial zonation of fault rocks in the ZF core, which they interpreted as reflecting an evolution from initial frictional deformation by cataclasis to a more distributed deformation style via the formation of a thoroughly overprinting phyllonitic fabric in the core. This progressive evolution was interpreted as suggesting that initial pervasive cataclasis enhanced the overall system permeability, which would have enhanced the influx of CO_2-rich hydrous fluids that triggered low-grade alteration and the onset of pressure solution, leading to overall weakening, shear localization, and formation of talc-rich mylonitic layers in the fault core (this model has been further developed in Collettini et al., 2011; Collettini, 2011; Smith and Faulkner, 2010; Smith et al., 2011a, b). This, in turn, would have promoted rock weakening and a switch from frictional to an overall frictional–viscous fault behaviour (e.g. Collettini et al., 2009). Smith et al. (2011b) subsequently reported an alternative deformation history wherein the early development of mylonitic fabrics (talc phyllonite) was followed by the formation of cataclasite and breccia. The spatial zonation of fault rocks proposed by Smith and Faulkner (2010) and Smith et al. (2011b) is shown in Table 1.

Collettini and Holdsworth (2004) also stressed the role of the ZF as the main structure accommodating the late Neogene upper crustal extension in the Northern Apennines and proposed a possible mechanical explanation for its development as a LANF. Although the ZF is traditionally described and interpreted as a subhorizontal to gently dipping top-to-the-east LANF, Musumeci et al. (2015) proposed an alternative model wherein the exposed ZF represents the flat of a much larger, out-of-sequence top-to-the-east thrust that cuts through the eastern Elba nappe stack. The same authors bracketed the activity of the ZF to between 6.23 ± 0.06 and 5.39 ± 0.46 Ma, based on the youngest available muscovite ^{40}Ar / ^{39}Ar age from the footwall and a U–Th–He age on adularia and hematite mineralizations in the hanging wall (e.g. Lippolt et al., 1995). Viola et al. (2018) provided the first absolute dating of part of the fault activity, constraining the age of the gouge associated with the ZF PSS to < 4.9 Ma, consistent with the fundamental observation that the fault gouge and cataclasite contain clasts of the monzogranitic Porto Azzurro pluton dated to ca. 6.5 Ma (e.g. Gagnevin et al., 2011; Musumeci et al., 2015).

Table 1. Definition of brittle structural facies in this work and comparison with existing classifications of the various fault rocks associated with the ZF. Colours correspond to those of Fig. 2.

Smith & Faulkner, 2010	Smith et al., 2011	This work
L5 gouge; foliated breccia	L5 gouge; breccia	BSF1 yellowish cataclasite and gouge
L4 foliated cataclasite	L4 foliated cataclasite; reworked phyllonite	BSF2 yellowish foliated cataclasite
L3 chlorite phyllonite; talc phyllonite; amphibole schist	L3 calcite mylonite; talc phyllonite; talc-tremolite phyllonite	BSF3 calcite mylonite; talc phyllonite; talc tremolite phyllonite
L2 amphibole schist	L2 tremolite schist	BSF4 cohesive greenish cataclasite
L1 breccia	L1 footwall breccia	BSF5 massive cataclasite (honeycomb breccia)
		BSF6 lower quartzitic breccia
footwall	footwall	Footwall quartzite and mylonitic marble

5 Results

5.1 Zuccale Fault: internal architecture, BSF definition, and characterization

The most complete and continuous exposure of the ZF is easily accessible and well exposed along two coastal cross sections oriented N–S and E–W at Punta Zuccale (Figs. 1b and 2). There, the ZF zone is between ca. 1.5 and 3 m thick, and it discordantly cuts across both the footwall (quartzite and andalusite-bearing spotted schist) and the hanging wall (marly Cretaceous flysch). Overall, ZF fault rocks consist of clast and/or matrix-supported breccia and cataclasite exhibiting large lateral variations in thickness, texture, and composition (Musumeci et al., 2015). Gouge exists as 2–10 cm thick discontinuous lenses across the fault zone but is particularly common at or close to the upper boundary of the fault zone, i.e. immediately below the hanging wall block. Two slivers of mylonitic marble derived from the footwall block (Calanchiole marble; Musumeci and Vaselli, 2012; Musumeci et al., 2015; Viola et al., 2018) are embedded within the fault zone.

Detailed field mapping and multiscalar fault rock characterization has allowed us to refine the detailed characterization of the ZF structural framework and to distinguish and characterize five distinct BSFs, the distribution of which is shown in map view, and by means of a fence diagram in Fig. 2a and b and listed in Table 1. BSFs are numbered according to their geometrical position from the top to the base of the ZF, as observed along the two natural and mutually orthogonal cross sections (see fence diagram in Fig. 2b). Their identification and characterization have steered the sampling strategy to obtain (when possible) absolute illite K–Ar time constraints, as discussed below.
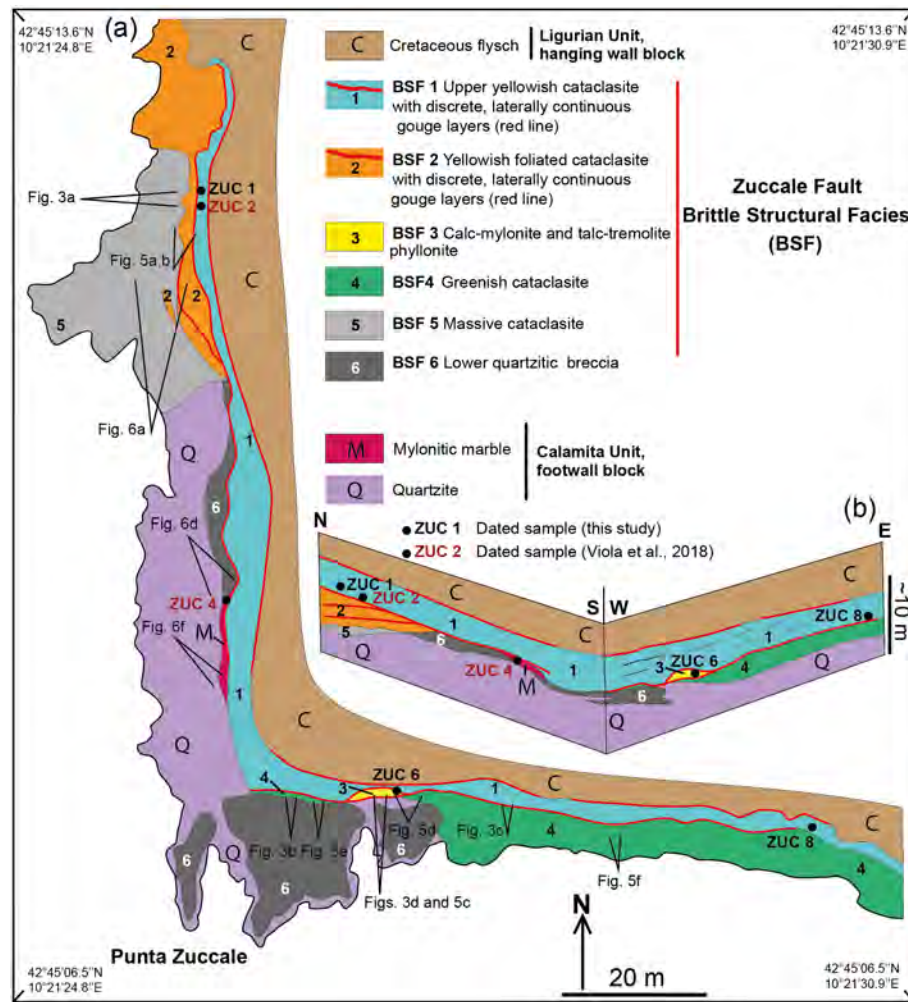
Figure 2. (a) Geological map of Punta Zuccale showing the distribution of the brittle structural facies (BSF) of the ZF and the location and name of the samples dated in this study (in black) and in Viola et al. (2018; in red). The location and direction of view of the photographs in Figs. 3, 5, and 6 are shown. **(b)** Fence diagram illustrating fault rock distribution along the N–S and E–W natural cross sections that are directly accessible along the shoreline of Punta Zuccale.

5.1.1 BSF 1 – upper yellowish cataclasites

A yellowish cataclasite represents the uppermost portion of the ZF core. It crops out continuously below the hanging wall Cretaceous flysch, which is, in turn, itself characterized by a decimetric to metric damage zone defined by increased fracture density and foliated domains with localized S/C fabrics confirming the regional top-to-the-east sense of shear of the ZF. BSF 1 rests immediately above the striated PSS of the ZF (see below) and is composed of a few discrete, centimetre-thick ultracataclasite and gouge bands. It exhibits a subhorizontal contact to the hanging wall block (Fig. 3a, b). Discrete top-to-the-east striated fault planes cut across the fault rocks of BSF 1. Cataclastic bands are composed of cohesive to poorly lithified yellowish cataclasite (Fig. 3c) containing angular to subrounded clasts with sizes from centimetres to millimetres. Clasts are mainly of limestone, quartzite, and ig-

neous rocks (leucogranite sill) commonly replaced or altered by secondary carbonate grains and of pyrite-bearing veins. The fine-grained to very fine-grained matrix ($< 50\,\mu m$) of the cataclasite consists of secondary dolomite, calcite, quartz, clay minerals, and Fe oxides. Secondary dolomite and calcite also occur as euhedral crystals and/or filling of veins (Fig. 4a, b). At the mesoscopic scale, a poorly developed and gently ($< 20°$) west-dipping foliation (Fig. 3c) is recognized. It is crosscut by centimetre-spaced and millimetre-thick subhorizontal fault planes dipping gently ($< 5°$) toward the west (Fig. 3c). The basal portion of BSF 1 consists of greenish, cohesive, and strongly indurated matrix-supported cataclasite containing foliated to non-foliated millimetre- to centimetre-thick gouge bands. In the gouge, clasts are represented by rounded quartz grains and/or breccia grains. At the optical microscope, the foliation appears as defined by thin (1 mm) and discontinuous clay mineral-rich layers that

outline a centimetre spaced, subhorizontal, or gently dipping foliation, while dolomite and calcite occur as recrystallized grains (Fig. 4a). BSF 1 contains clear top-to-the-east kinematic indicators such as oblique fabrics, S/C-type shear bands, and asymmetric imbricated sigmoidal lithons also derived from other BSFs (e.g. Fig. 3b).

5.1.2   BSF 2 – foliated yellowish cataclasites

This foliated cataclasite occurs in the northernmost exposed ZF, where it is sandwiched between BSF 1 above and BSF 5 below (Fig. 3a), and it tapers off progressively towards the south (Fig. 2a, b). BSF 2 fault rocks appear as a cohesive foliated whitish–yellowish cataclasite in the immediate footwall of the ZF striated PSS (Fig. 5a, b). The PSS and subparallel striated planes dip gently to the west (Viola et al., 2018, their Fig. 3). W-plunging slickenlines are associated with slickensides and other kinematic indicators (i.e. S/C-type shear bands in the foliated cataclasite) and are consistent with a top-to-the-east sense of shear. The cataclasite is made of centimetric, rounded to subangular clasts (Fig. 4c and d) in a fine-grained foliated matrix containing secondary dolomite and calcite, clay minerals, and amorphous silica pockets. Clasts are mainly derived from the hanging wall Cretaceous flysch and from late Miocene leucogranite sills hosted in the flysch (Viola et al., 2018). The rare occurrence of quartz and/or phyllite clasts (Fig. 4d) indicates a contribution also from the footwall metamorphic Triassic Verrucano Formation (Fm.) quartzite and metapelite. The NNE-striking cataclastic foliation dips gently ($< 30°$) to the west and bears E–W-trending slickenlines. A noteworthy feature of the BSF 2 cataclasite is the abundance in the matrix of Fe oxides (ilmenite), along with the occurrence of decimetre-thick sulfide (pyrite, galena, sphalerite) and Fe-oxide-rich layers at the contact with the underlying BSF 5 cataclasite (Gundlach-Graham et al., 2018).

5.1.3   BSF 3 – calcite mylonite and talc-smectite-tremolite phyllonite

This BSF corresponds to a 10 m long and 1–3 m thick lensoidal body made of calc-mylonite and greenish talc-smectite-tremolite phyllonite (Fig. 3d). The unit is bounded at the top and at the base by discrete yellow gouge layers and greenish cataclasite that can be ascribed to BSF 1 and BSF 4, respectively. The phyllonitic component consists of a serrated alternation between well-foliated white and greenish bands that are centimetres to tens of centimetres thick and that reflect a compositional layering made up of calcite-, talc-smectite-tremolite-, and phyllosilicate-rich layers (Figs. 3d and 5c). At the thin-section scale, the fabric is characterized by fine-grained calcite lithons interspersed within a network of thin (< 1 mm) smectite- and/or talc-rich layers (Fig. 4e and f) that define a well-developed foliation with millimetric spacing in high strain zones (see Collettini et al., 2009, for a

detailed mechanical and microstructural characterization of this fault rock).

5.1.4   BSF 4 – greenish cataclasites

BSF 4 is only exposed along the southern, E–W section, as it tapers completely out moving north (Fig. 2a, b). It varies in thickness from a few centimetres up to 1 m. Its basal contact discordantly cuts across the west-dipping foliation of the footwall rocks, which are cordierite- and biotite-bearing hornfels and quartzite breccia formed at the expense of the underlying footwall Calamita Unit. Fault rocks appear as a cohesive and strongly indurated, matrix-supported cataclasite (Figs. 5e, 4g, h) containing angular clasts of quartzite, amphibole- and plagioclase-bearing skarn, epidote-bearing veins, and reworked older breccia and cataclasite. Clasts range in diameter from a few millimetres to a few centimetres, with the coarsest clasts mainly localized in up to decimetre-thick breccia pockets and/or coarse-grained cataclasite layers. Millimetric clay-rich layers locally define a coarsely spaced subhorizontal or gently dipping foliation. Dark green to rust brown foliated to non-foliated gouge occurs as millimetre- to centimetre-thick discontinuous layers (Fig. 5f) with sharp contacts to the contiguous breccia and cataclasite (Fig. 4g). In the gouge, the clasts are represented by rounded quartz grains and/or older breccia clasts. The clasts define a weak shape-preferred orientation (SPO) that is generally parallel to the gently dipping foliation of the clay-rich layers.

5.1.5   BSF 5 – massive cataclasites

BSF 5 crops out in the northernmost portion of the ZF (Figs. 2a, 6a, b). It is characterized by significant thickness variations, lobate and digitate contacts with the footwall Triassic quartzites, and an overall 3D wedge shape that tapers towards the south. It is a matrix-supported cohesive and strongly indurated greyish to whitish cataclasite referred to as "honeycomb breccia" in the literature (Smith et al., 2008; Fig. 6c). Coarse- to medium-grained subrounded to angular quartz, phyllite and hornfels clasts are embedded in an isotropic matrix devoid of any internal fabric and composed of very fine-grained quartz, clay minerals, and epidote (Fig. 6c). Locally, the greenish colour is due to the great abundance of epidote in the matrix. The massive cataclasite rests directly on Verrucano Fm. quartzites (Fig. 2), and centimetre- to decimetre-thick slices of quartzites are locally embedded as clasts within the basal massive greyish cataclasite. At the thin-section scale, the original rock fabric (quartz clasts and matrix) is partially replaced by the growth of secondary dolomite. Clasts form a very weak SPO in this BSF, which is generally roughly perpendicular to the gently dipping foliation of the overlying BSF 2 and principal slip surface.
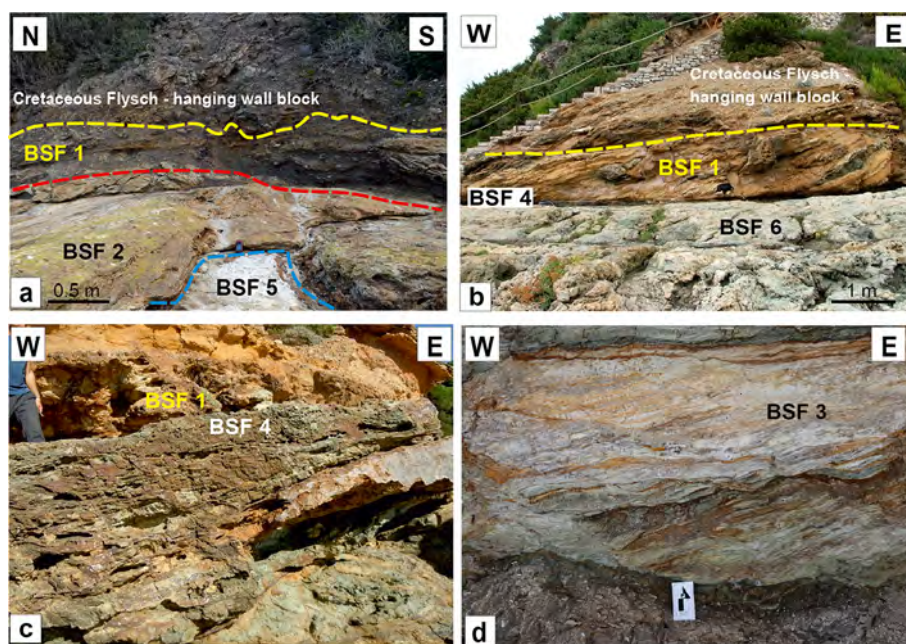
Figure 3. Field view of selected BSFs. Panels **(a)** and **(b)** show examples of the complex internal architecture of the ZF with the tight juxtaposition of several BSFs. **(a)** Northernmost exposed portion of the fault, allowing access to an almost complete section of the fault zone. There the ZF is composed of a stack of three different BSFs and the hanging wall block on top. **(b)** Sharp contact at Punta Zuccale between unit BSF 1 and BSF 6 separated by a thin layer of BSF 4. Note the mesoscale evidence of tectonic imbrication within BSF 1 indicating top-to-the-east transport. This is not obvious in **(a)**, as the view there is in the direction of transport. **(c)** Detail of BSF 1 (above) to BSF 4 (below) contact. **(d)** Pervasively foliated phyllonitic BSF 3.

5.1.6 BSF 6 – lower quartzitic breccia

BSF 6 represents the structurally lowermost BSF of the complex ZF internal architecture. It occurs as discontinuous decametric bands of white breccias at the top of Triassic Verrucano Fm. quartzite footwall rocks (Fig. 2). It is formed by a matrix-supported, cohesive greyish to whitish breccia and cataclasite (Fig. 6d and e). Coarse- to medium-grained subrounded to angular quartz, phyllite, and hornfels clasts are embedded in a massive matrix that consists of very fine-grained quartz, clay minerals, and epidote. The cataclasite directly rests on the quartzite and cordierite- and biotite-bearing schist of the footwall Verrucano Fm. (Fig. 6e), with the local presence of discrete centimetric to decimetric slices of quartzites at the base of the BSF 4 lower massive cataclasite. At the thin-section scale, quartz clasts and the matrix are both characterized by the widespread growth of secondary dolomite grains that partially overprint or replace the original cataclastic fabric. Similarly to BSF 5, the locally well-developed clast SPO is at a steep angle (80–85°) to the weak and gently dipping foliation of the overlying BSF 4 cataclasite.

5.1.7 Footwall of the Zuccale Fault

Footwall rocks are well exposed along the N–S section and mainly consist of white quartzite of the Verrucano

Fm. (Fig. 6f) and biotite- and cordierite-bearing schists that become dominant north of the investigated Zuccale section (Musumeci and Vaselli, 2012). Above the cordierite-bearing schist, a white calcite mylonitic marble with greenish amphibole- and epidote-bearing calc–silicate is exposed for a length of several metres and is discordantly capped by BSF 1 (Fig. 6). This high-strain marble has been interpreted as coring the Calanchiole Shear Zone (e.g. Musumeci and Vaselli, 2012), a 40–45° west-dipping and top-to-the-east brittle–ductile thrust. The marble is interpreted as Jurassic in age and is characterized by a penetrative N–S-striking mylonitic fabric. Deformation therein has been dated to 6 Ma (Viola et al., 2018), which attests to lower amphibolite–upper greenschist facies ductile deformation with dynamic recrystallization of calcite grains, together with synkinematic growth of fine-grained tremolite and talc within the thermal aureole of the Porto Azzurro pluton (Musumeci et al., 2015).

5.2 ZF samples and K–Ar dating results

Aiming to further constrain the development of the ZF fault architecture and to add absolute time constraints to it, and thus strengthening the initial results reported by Viola et al. (2018), we sampled and dated all the BSFs described above. Unfortunately, only two BSFs yielded datable material.
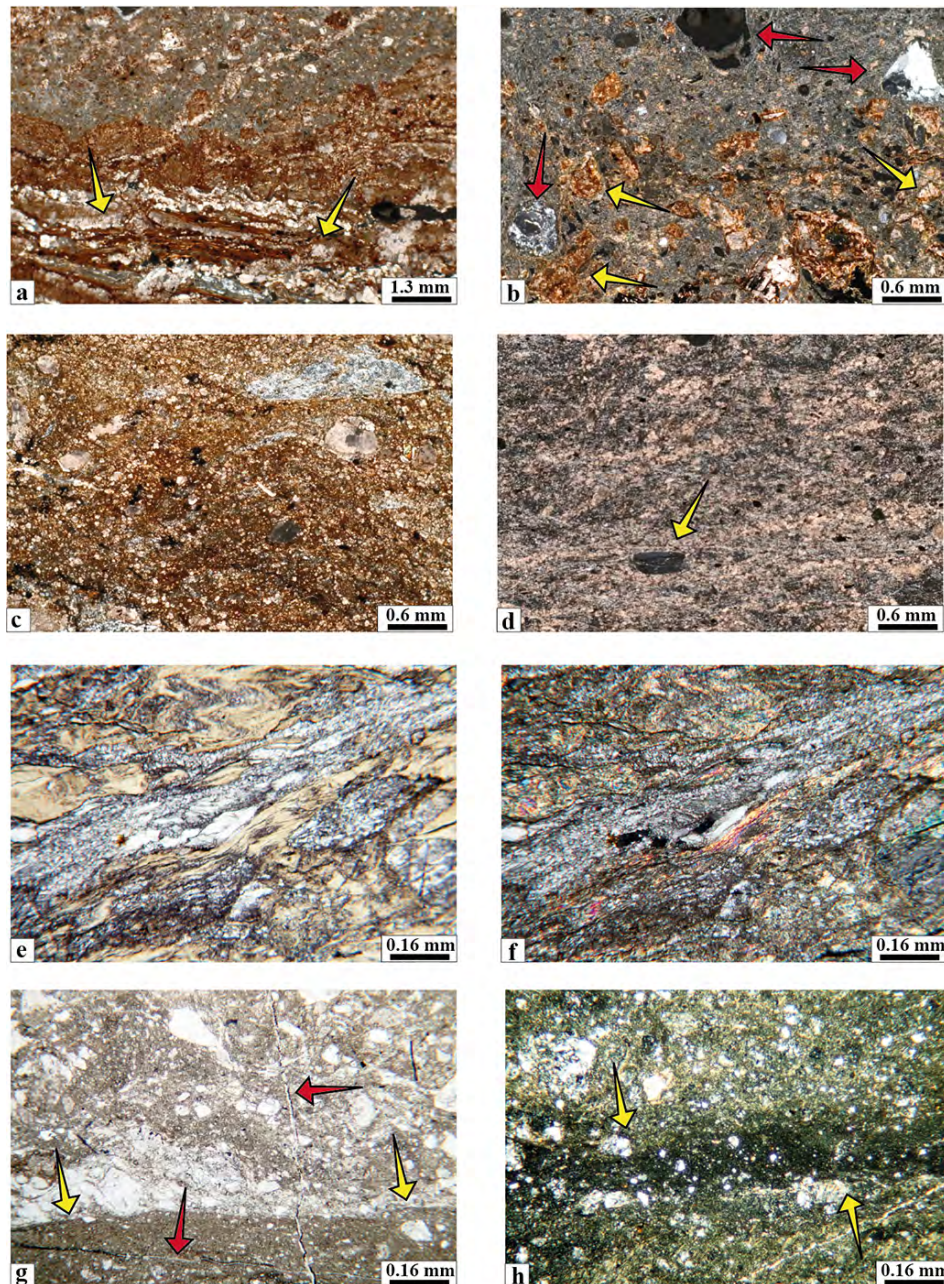
Figure 4. Microphotographs of representative examples of BSF fabrics. Panels **(a–b)** show BSF 1. **(a)** Very fine-grained matrix with extensive crystallization of secondary calcite and dolomite with sparse embedded euhedral dolomite grains (grey layer, upper half of photo) and Fe oxide and hydroxide alteration (reddish layer, lower half of photo). Relic foliated cataclastic domains (indicated by the yellow arrows) alternate with Fe hydroxide bands and dolomite veins shown using plane polarized light (PPL). **(b)** Cataclasite with rare quartz–feldspar clasts (red arrows) in a very fine-grained matrix characterized by diffuse recrystallization of secondary calcite and dolomite (lower half of the photo) also occurring as euhedral grains (yellow arrow) shown using crossed polarized light (CPL). Panels **(c–d)** show BSF 2. **(c)** Foliated cataclasite with preserved fine-grained quartz clasts and carbonate euhedral grains. The fine-grained matrix consists of secondary calcite shown using PPL. **(d)** Very fine-grained phyllosilicate-, calcite-, and dolomite-rich cataclasite matrix enveloping phyllite clasts (yellow arrow). Diffuse occurrence of coarse-grained secondary calcite in the upper half of photo shown using CPL. Panels **(e–f)** show BSF 3. **(e)** Very fine-grained talc phyllonite; talc-serpentine-rich yellowish layers alternate with whitish very fine-grained (10–15 μm) calcite-rich layers shown using PPL. Panel **(f)** is the same image as **(e)** but using CPL. Panels **(g–h)** show BSF 4. **(g)** Clast-rich foliated cataclasite with a very fine-grained phyllosilicate-rich matrix (upper half of photo) in sharp contact with matrix-rich ultracataclasite marked by significant grain size reduction and well-rounded clasts (yellow arrows). Very thin calcite veins cut across the cataclasite fabric (red arrows) shown using PPL. **(h)** Quartz–feldspar cataclasite with a very fine-grained phyllosilicate-rich matrix, enclosing a very thin (100–150 μm) ultracataclasite layer (yellow arrows) shown using CPL.
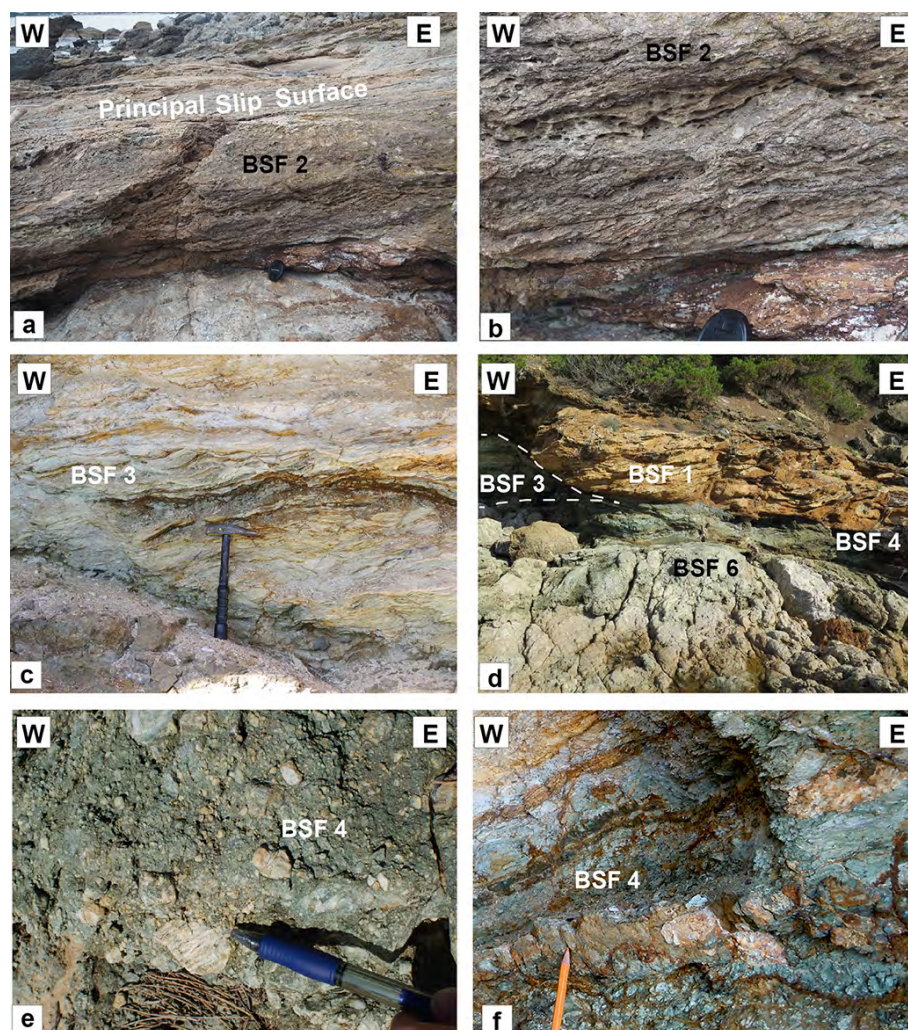
Figure 5. Outcrop view of fault rocks from different BSFs. Panels **(a, b)** show BSF 2. **(a)** Upper yellowish cohesive cataclasite with gently W-dipping foliation capped by the subhorizontal ZF principal slip surface. **(b)** Detail of foliated cataclasite with oblique foliation indicating top-to-the-east shearing. **(c)** Compositionally banded phyllonite of BSF 3. Note the shear bands constraining top-to-the-east shearing along the subhorizontal foliation. **(d)** Outcrop view of the complex spatial arrangement of four different BSFs at the western termination of the E–W section at Punta Zuccale. Note the eastern lateral closure of BSF 3, which forms a metric lens in the complex architecture of the ZF (see Fig. 2). The width of the photograph corresponds to ca. 8–10 m. **(e)** BSF 4 greenish cataclasite with millimetric angular to subrounded quartz clasts deriving from underlying Triassic quartzites in a very fine-grained matrix made up of ultracataclasite and gouges. **(f)** Detailed view of a foliated gouge level within BSF 4.

5.2.1 ZUC 1 (BSF 1)

This sample is from the N–S-trending section at Punta Zuccale and is representative of the yellowish cataclasites of BSF 1. The dated material rests directly upon the striated ZF PSS that bears E–W-trending and W-plunging slickenlines and is composed of a matrix-supported, clay-rich yellowish gouge formed at the expense of the hanging wall Cretaceous flysch (Fig. 7). The sampled gouge is internally chaotic, is devoid of any internal fabric, and does not exhibit any consistent indication of a specific sense of shear (Fig. 7). The kinematics, however, are clearly constrained by a plethora of top-to-the-east kinematic indicators associated with the slip recorded along the discrete ZF PSS immediately at the base of ZUC 1, such as slickenside surfaces or the dragging of foliated cataclasites of BSF 2 into the slip plane.

Concerning the mineralogical composition of the investigated sample, the 2–6 and 6–10 µm grain size fractions of gouge ZUC 1 are mainly composed of quartz (38 %–41 %); carbonate minerals (dolomite and aragonite, between 15 % and 27 %); illite-2M$_1$ (14 %–17 %); and subordinate amounts of illite-1M$_d$ (6 %–7 %), kaolinite (6 %–9 %), and mixed layers of illite-smectite (I–S; 5 %–7 %). Low halite (4 %) con-
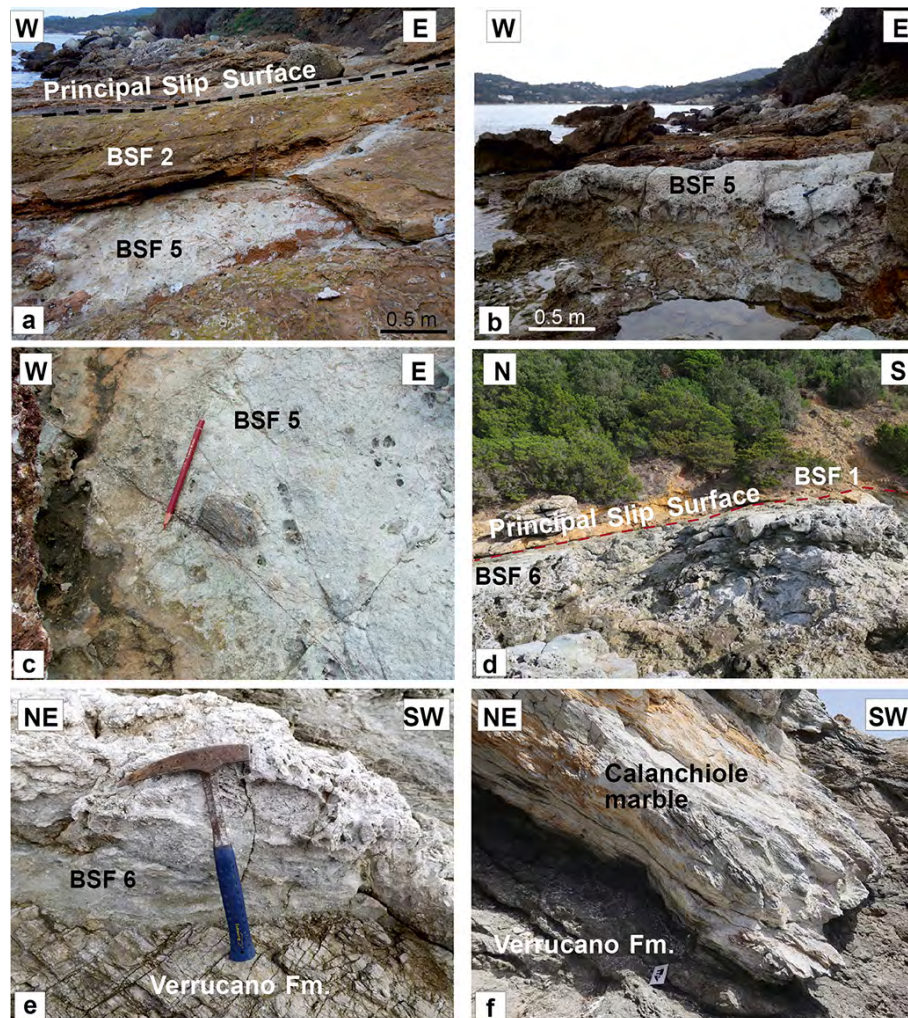
Figure 6. (a) BSF 5 upper contact to the foliated cataclasite of BSF 2. The latter is truncated by the ZF principal slip surface. **(b)** The distinctive look of the lower massive greyish to whitish cataclasite exhibits a honeycomb texture as result of clast erosion. **(c)** Detail view of centimetre-sized clasts, varying from subrounded quartz to angular hornfels slate embedded in a massive fine- to medium-grained matrix. **(d)** BSF 6 in the immediate footwall of the ZF PSS along the N–S section at Punta Zuccale. The image is ca. 5 m in width. **(e)** Outcrop view of decimetric layers of the BSF 6 whitish to greyish lower breccia resting above the Triassic quartzite of the Verrucano Fm. **(f)** W-dipping foliated marble of the Calanchiole shear zone in the footwall of the ZF.

tents, likely reflecting aerosols from seawater, have also been detected in the coarse fractions.

Quartz and kaolinite become less abundant in the fine fractions (0.1–0.4, 0.4–2 µm), where a general increase of illite-$1M_d$, illite-$2M_1$, and mixed layers of I–S is instead observed passing from 13 %–37 %, from 27 %–41 %, and from 7 %–11 %, respectively (Fig. 7, Table 1).

Importantly, this sample is from the same sampling site as sample ZUC 2 reported by Viola et al. (2018), which constrained faulting at this locality to < 4.9 Ma.

5.2.2   ZUC 8 (BSF 1)

Sample ZUC 8 is also from BSF 1, but it is from the easternmost exposed tract of the E–W-trending section of the ZF

(Figs. 2 and 7). It represents chestnut brown gouge lenses, which are internally devoid of any pervasive fabric and interfingered with yellowish cataclasite and gouge. The latter is pervasively foliated and contains abundant kinematic indicators such as asymmetric and imbricated clasts and lenses and oblique planar fabrics indicating top-to-the-east shearing.

The coarse grain size fractions (2–6 and 6–10 µm) of gouge ZUC 8 contain kaolinite amounts varying between 46 % and 51 % of the overall composition, followed by illite-$2M_1$ (22 %–24 %), quartz (11 %–19 %), and chlorite (13 %–14 %). The lack of quartz grains and the general decrease of kaolinite contents in the finer grain size fractions (< 0.1, 0.1–0.4, 0.4–2 µm) are compensated for by an increase of neo-formed illite-$1M_d$, as well as chlorite and illite-$2M_1$ (Fig. 7).
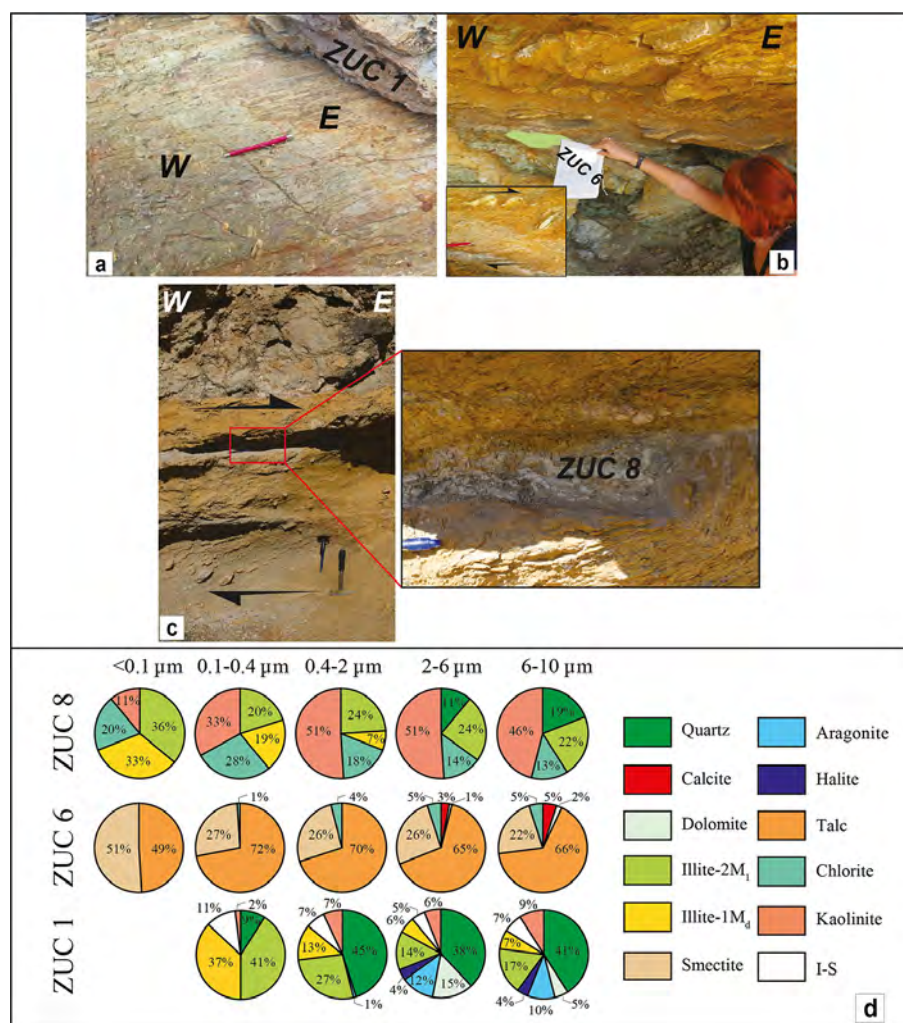
Figure 7. (a–c) Sampled fault rocks and associated mesoscopic structures. ZUC 1 is from BSF 1 and comes from the immediate hanging wall of the ZF principal slip surface, which is decorated by pervasive E–W striae. ZUC 6 is from the uppermost part of BSF 3, which contains very clear top-to-the-east kinematic indicators. ZUC 8 is from the easternmost exposed BSF 1, where clear top-to-the-east kinematic indicators occur. **(d)** Mineralogical composition of the separated grain size fractions of the three dated samples.

5.2.3 ZUC 6 (BSF 3)

This sample is from the E–W-trending section of the ZF (Fig. 2), and it was taken from the uppermost part of the talc-tremolite phyllonitic lens forming BSF 3 (Fig. 7). The dated material is composed of fine-grained, yellowish to greenish phyllonite that in the field appears as made of massive calcite-rich sigmoidal lithons and lenses dispersed within a weakly foliated matrix made of tremolite and phyllosilicate. ZUC 6 is from "zone L2" by Collettini et al. (2009). XRD analysis of the sample indicates talc and smectite as the major constituents of the sub-fractions, with contents ranging from 49 %–72 % and from 22 %–51 %, respectively (Fig. 7, Table 1). The coarser grain size fractions (6–10 and 2–6 μm) also contain minor amounts of chlorite (5 %), calcite (3 %–5 %), and dolomite (1 %–2 %) that become progressively less abundant or totally disappear in the finer fractions (< 0.1, 0.1–0.4, 0.4–2 μm; see Fig. 7). Smectite is the dominant K-bearing clay mineral in the < 0.1 μm fraction, forming 51 % of the whole-rock mineralogical assemblage.

It needs to be pointed out that it was not possible to obtain any material from the collected samples of BSF 2, 4, 5, and 6. Many attempts to disaggregate the cataclasite of those BSFs failed, and thus no datable grain size fractions could be separated from these indurated fault rocks.

5.2.4 K–Ar dating results

Our dataset almost invariably exhibits a "grain size–age correlation" for the three samples, wherein the coarser the dated grain size fraction, the older the age (Fig. 8).

While only four size fractions were analysed by K–Ar geochronology for ZUC 1, as no < 0.1 μm grain size fraction could be separated, five fractions were successfully dated for ZUC 6 and ZUC 8 (Table 3 and Fig. 8). For sample ZUC 1, the < 0.4 μm finest obtained fraction yields a date of 18.8 ± 0.3 Ma, the 0.4–2 μm fraction yields a date of 28.2 ± 0.4 Ma, and the 2–6 μm fraction and the 6–10 μm split yield two identical dates of 34.2 ± 0.5 Ma. Sample ZUC 8 yielded K–Ar dates of 23.7 ± 0.4, 34.4 ± 0.5, 59.7 ± 0.9, 151 ± 2.3, and 155.7 ± 2.4 Ma for the < 0.1, 0.1–0.4, 0.4–2, 2–6, and 6–10 μm splits, respectively. For sample ZUC 6, the < 0.1 μm split yielded a date of 21.0 ± 2.1 Ma, with dates becoming progressively older at 40 ± 2.8, 47.4 ± 3.0, 40.6 ± 3.2, and 61.6 ± 4.4 Ma for the 0.1–0.4, 0.4–2, 2–6, and 6–10 μm splits, respectively.

TEM imaging integrated the characterization of the dated fractions, particularly of the finest fractions, which are interpreted as providing the tighter constraint upon the last slip episode recorded by the dated fault rock (see below for details). As noted, sample ZUC 1 did not yield any datable material for the finest fraction, and thus no TEM investigations were carried out. We can rely, however, on observations from sample ZUC 2 by Viola et al. (2018), taken in the same BSF only a couple of metres away in the along-strike direction from ZUC 1 (Fig. 4c and d by Viola et al., 2018). Two generations of illite crystals were recognized in the finest ZUC 2 fraction, with an acicular and platy shape, respectively.

Sample ZUC 8 contains illite platelets with irregular edges (Fig. 8) similar to those documented for ZUC 2 by Viola et al. (2018) and inferred for ZUC 1 in this study.

TEM imaging and energy dispersive X-ray spectroscopy (EDS) of the finest fraction of ZUC 6 confirms the abundant presence of K-bearing smectite crystals, as documented by the XRD analysis (Figs. 7 and 8).

6　Discussion

Our results are first discussed and interpreted in general terms, aiming to assess their impact upon a conceptual model for the time-integrated development of the ZF. This is important for understanding the broader context of brittle faulting and deformation localization during long-lived structural evolutions and upon the methodological approach to studying and unravelling complex fault cores. Finally, we discuss the significance of our study upon the tectonic evolution of the eastern Elba nappe stack and in the framework of the Northern Apennines evolution.

6.1　Interpretation of the age results

The new data depict a complex history "archived" within the ZF fault core at the studied outcrop (Fig. 8). The obtained "K–Ar age vs. grain size" relationship is remarkable, with the

three dated samples yielding quite different results and being characterized by heterogeneous "age vs. grain size spectra" (sensu Pevear, 1999), wherein the coarser the fraction, the older the age. In this study, we use the "Age Attractor Model (AAM)" first proposed by Torgersen et al. (2015a) and Viola et al. (2016) to interpret the obtained age data. The AAM suggests that the amount of detrital K-bearing phases inherited from the host rock in a brittle fault rock decreases with the decreasing grain size of the dated fractions, whereas the amount of authigenic and synkinematic clay increases with decreasing grain size. The coarsest dated fractions may thus still contain significant amounts of "old" protolithic K-bearing minerals inherited from the host rock. These grain size fractions are unrelated or only partly related to the faulting history we are interested in dating, leading to spurious ages. In the intermediate size fractions, a mixture of protolithic and authigenic illite would ensue, such that their dates also do not necessarily reflect the timing of fault initial slip or subsequent reactivation and are instead mostly devoid of geological meaning. On the other hand, although according to the AAM even the finest dated fractions may be partly contaminated by the host rock or may have experienced some degree of partial overprinting and resetting by younger tectonic and thermal events, many studies have convincingly shown that the age of the finest fractions (< 0.1 μm or finer) is a reliable record of the timing of the last brittle deformation increment recorded by the fault (Viola et al., 2013, 2016; Torgersen et al., 2015a, b; Mancktelow et al., 2015; Aldega et al., 2019; Scheiber et al., 2019; Curzi et al., 2020a, b; Tartaglia et al., 2020). Only in the ideal case, where all K–Ar ages from one sample are statistically identical for all dated grain size fractions, is it possible to assume that the age of the finest fraction and of all other fractions represents the true age of the last recorded faulting event, without any input from "old" protolithic components (see, for example, ELB 2 and ZUC 4 by Viola et al., 2018; Fig. 8; Torgersen et al., 2015a).

The contribution of potential host rock contamination, particularly in low-temperature fault rocks reworking sedimentary rocks and containing significant amounts of illite derived from the sedimentary history of the faulted lithology, may be evaluated with the Illite Age Analysis (IAA) approach (e.g. Hunziker et al., 1986; Pevear, 1999; Aldega et al., 2019; Carboni et al., 2020; Curzi et al., 2020a). The IAA discriminates the mostly detrital $2M_1$ polytype (which in turn might represent a mixture of authigenic high-temperature illite and cataclastic, synkinematic muscovite) from a truly authigenic phase $1M_d$ formed synkinematically during faulting. The IAA, however, did not produce any meaningful dates in this study, yielding negative intercepts for 100 % $1M_d$, suggesting that the $2M_1$ polytype is also in part authigenic and synkinematic.

In accordance with the AAM approach, we thus base the interpretation of the new batch of age results mostly on the dates of the finest fractions as already done by Viola et
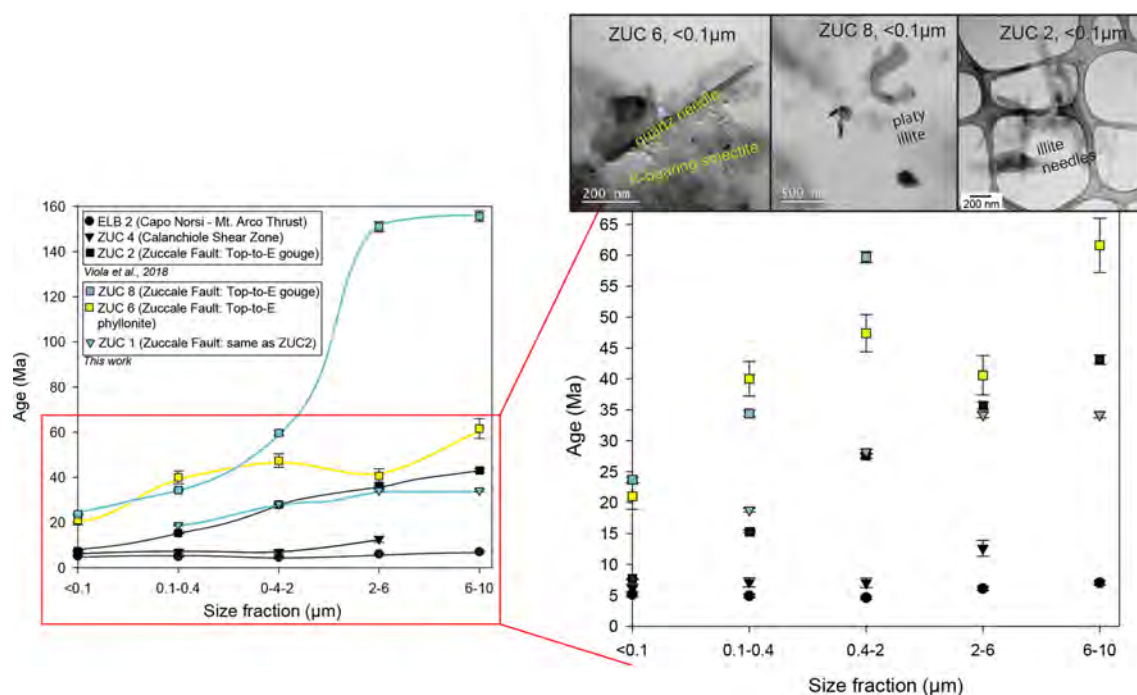
Figure 8. K–Ar age vs. grain size spectra for the three dated samples (in colour) compared and contrasted with the results by Viola et al. (2018) in black. **(b)** Selected transmission electron microscope images of the finest dated fractions of ZUC 6 and ZUC 8 from this study. The image of ZUC 2 is from Viola et el. (2018). Colours correspond to those used for the dated BSFs in Fig. 2.

al. (2018) for other samples from the ZF. We still consider them, however, as maximum ages of the last recorded increment of faulting because varying amounts of inherited K-bearing phases may still be present, thus potentially influencing the obtained apparent age.

Sample ZUC 1, for example, is indeed one such case, as discussed in depth for its companion ZUC 2 sample by Viola et al. (2018). It is a fault gouge formed at the expense of a compositionally heterogeneous flysch rock of Cretaceous age that is rich in siliciclastic inputs. In contrast to ZUC 2 in Viola et al. (2018), in the current study it was not possible to separate the $< 0.1\,\mu m$ grain size fraction of ZUC 1, such that the finest dated fraction is the $< 0.4\,\mu m$. It yielded a 18.8 ± 0.3 Ma date (Fig. 8). The age vs. grain size pattern of ZUC 1 is, however, very similar to that of ZUC 2 (Viola et al., 2018), with only minor differences except for the coarsest fraction. XRD analysis of ZUC 1 documents a mixture of roughly equal amounts of $1M_d$ and $2M_1$ illite polytypes in the finest dated fractions ($< 0.4\,\mu m$; Table 2). This is consistent with results from detailed scanning electron microscope (SEM) and TEM imaging of ZUC 2 (Fig. 8 and Viola et al., 2018), which disclosed the presence of two different generations of illite within this gouge, with a detrital component coexisting to varying degrees in different size fractions with authigenic and synkinematic illite crystals. Although the age of the $< 0.1\,\mu m$ fraction of ZUC 1 is unknown, one might extrapolate the sample age vs. grain size trend to an hypothet-

ical date by mimicking the slope of the trend of the ZUC 2 companion sample by Viola et al. (2018), ending up with a < 10 Ma age for the finest fraction. Irrespective of the exact date, the extrapolated result is still likely to be spurious as the fraction is known to contain old and protolithic illite, which makes the date artificially older. To account for this, Viola et al. (2018) calculated a modelled age for ZUC 2 of < 4.9 Ma by removing various amounts of "old" contaminant phyllosilicates with varying K content that represent detrital input into the gouge formed by either inherited illite, illite-smectite, or muscovite. In line with that modelling approach and the obtained results, we, therefore, consider a < 4.9 Ma age reasonable for also ZUC 1.

Samples ZUC 8 and ZUC 6 are strikingly different from ZUC 1 and, when considering the coarse fractions, also from each other. Their finest fractions, instead, yielded statistically identical dates, both constraining the same deformation event in the Aquitanian, between 21 and 23 Ma ago. As discussed above, K-bearing smectite is the dated mineral in sample ZUC 6, with its content progressively increasing to a maximum of 51 % of the total fraction in the finest fraction, corroborating its authigenic origin. ZUC 8, on the other hand, is compositionally more heterogeneous than ZUC 6, with both $2M_1$ and $1M_d$ illite polytypes contributing to the age of the finest fraction. Thus, the "convergence" to the same Aquitanian age is indeed remarkable, with the ca. 155 Ma age of the coarsest fraction of ZUC 8 more than twice as old as

Table 2. Mineralogical composition of various grain size fractions for gouges of the ZF. Qtz stands for quartz, Cal stands for calcite, Dol stands for dolomite, Arg stands for aragonite, Hl stands for halite, Tlc stands for talc, I-2M1 stands for illite–muscovite-2M1, I-1Md stands for illite-1Md, Sm stands for smectite, I–S stands for mixed layers of illite–smectite, Chl stands for chlorite, and Kln stands for kaolinite.

Sample (fraction size in µm)		Whole-rock composition (wt %)											
		Qtz	Cal	Dol	Arg	Hl	Tlc	I-2M$_1$	I-1M$_d$	Sm	I-S	Chl	Kln
ZUC 8	6–10	19	–	–	–	–	–	22	–	–	–	13	46
ZUC 8	2–6	11	–	–	–	–	–	24	–	–	–	14	51
ZUC 8	0.4–2	–	–	–	–	–	–	24	7	–	–	18	51
ZUC 8	0.1–0.4	–	–	–	–	–	–	20	19	–	–	28	33
ZUC 8	< 0.1	–	–	–	–	–	–	36	33	–	–	20	11
ZUC 6	6–10	–	5	2	–	–	66	–	–	22	–	5	–
ZUC 6	2–6	–	3	1	–	–	65	–	–	26	–	5	–
ZUC 6	0.4–2	–	–	–	–	–	70	–	–	26	–	4	–
ZUC 6	0.1–0.4	–	–	–	–	–	72	–	–	27	–	1	–
ZUC 6	< 0.1	–	–	–	–	–	49	–	–	51	–	–	–
ZUC 1	6–10	41	–	5	10	4	–	17	7	–	7	–	9
ZUC 1	2–6	38	–	15	12	4	–	14	6	–	5	–	6
ZUC 1	0.4–2	45	–	–	1	–	–	27	13	–	7	–	7
ZUC 1	0.1–0.4	9	–	–	–	–	–	41	37	–	11	–	2

the age from the same grain size of ZUC 6. The meaning of the AAM approach is therefore self-evident when comparing these two samples, and this case study is reminiscent of other remarkable cases discussed in the literature, such as those by Torgersen et al. (2015b) and Viola et al. (2016). This strengthens our conclusion that the last recorded faulting increment did indeed "attract" the ages of the coarsest and remarkably different fractions to the same Aquitanian faulting age. The older ages are well preserved in discrete gouge lenses of BSF 1 and in BSF 3 along with specific metamorphic mineral assemblages (sample ZUC 6). A noteworthy feature of BSF 3 is that it is devoid of any pervasive brittle deformation and lacks evidence of fluid-driven deposition of secondary calcite / dolomite and Fe oxides / hydroxide, as instead commonly observed in BSF 1 and BSF 2 and to a lesser extent in BSF 4. This suggests that BSF 3 has behaved as an "across-foliation low-permeability barrier" during the ZF younger brittle deformation increments and fluid circulation, which is different from the other BSFs.

As a whole, the new dataset expands upon the dataset by Viola et al. (2018), who first documented a significant faulting age cluster in the early Pliocene. ZUC 6 and ZUC 8 now also document the coexistence in the ZF of fault rocks that, in addition to the Pliocene cluster, record a distinct thermotectonic event in the Aquitanian.

The new results allow us to evaluate and refine the available structural models for this major fault zone (e.g. Keller and Pialli, 1990; Keller and Coward, 1996; Collettini and Holdsworth, 2004; Collettini et al., 2009; Smith and Faulkner, 2010; Musumeci et al., 2015; Viola et al., 2018). The possibility to analytically demonstrate that the fault core

is composed of a range of coexisting BSFs that formed at significantly different times indeed calls for a re-evaluation of the existing evolutionary conceptual models.

The new data are of interest in that the kinematic framework of the fault does not appear to have changed from the Aquitanian to the Pliocene, with top-to-the-east transport remaining the regional kinematics along the fault (Collettini and Holdsworth, 2004; Collettini et al., 2009; Smith and Faulkner, 2010; Musumeci et al., 2015). However, our results indicate that, this consistency notwithstanding, the identified and sampled BSFs formed at very different times, with the phyllonitic fault rocks of BSF 3 and one gouge of BSF 1 both recording Aquitanian top-to-the-east faulting within a brittle–ductile regime. The second gouge from BSF 1 instead constrains Pliocene top-to-the-east faulting under entirely brittle conditions at shallow crustal level.

Any static or dynamic model ignoring or overlooking such fault internal heterogeneity is at risk to oversimplify the ZF evolution, potentially leading to erroneous conclusions as to its role in the local tectonic evolution or to unreliable inferences on the system mechanical behaviour.

6.2 General implications on workflows for the characterization of faults and on fault mechanics

The workflow presented here is of general interest to the structural geology and tectonics community as it demonstrates the need to carry out detailed structural and mechanical characterizations of brittle faults, while also keeping in mind the time dimension of faulting and the fact that currently side-by-side BSFs may actually be the product of de-

Table 3. K–Ar data of the three analysed samples.

Sample name	Fraction (μm)	Mass (mg)	Radiogenic $^{40}Ar^*$			K			Age data	
			mol g^{-1}	σ (%)	$^{40}Ar^*$ (%)	Mass (mg)	wt %	σ (%)	Age (Ma)	σ (Ma)
ZUC 1	0.1–0.4	3.284	1.704×10^{-10}	0.42	30.1	50.5	5.206	1.53	18.8	± 0.3
	0.4–2	3.314	1.895×10^{-10}	0.39	43.5	51.7	3.849	1.52	28.2	± 0.4
	2–6	4.35	1.414×10^{-10}	0.39	46.0	50.4	2.365	1.53	34.2	± 0.5
	6–10	4.32	1.718×10^{-10}	0.35	43.6	52.3	2.870	1.52	34.2	± 0.5
ZUC 6	< 0.1	3.562	2.228×10^{-12}	8.61	2.6	12.8	0.061	5.15	21.0	± 2.1
	0.1–0.4	19.398	9.116×10^{-13}	4.78	0.4	50.2	0.013	5.01	40.0	± 2.8
	0.4–2	17.948	1.11×10^{-12}	3.76	0.5	48.9	0.013	5.01	47.4	± 3.0
	2–6	14.03	8.188×10^{-13}	6.09	0.4	49.2	0.012	5.01	40.6	± 3.2
	6–10	12.712	1.162×10^{-12}	5.03	0.6	55.5	0.011	5.01	61.6	± 4.4
ZUC 8	< 0.1	2.824	1.777×10^{-10}	0.46	35.4	51.3	4.302	1.53	23.7	± 0.4
	0.1–0.4	2.378	2.573×10^{-10}	0.42	49.8	49.5	4.273	1.53	34.4	± 0.5
	0.4–2	3.084	3.967×10^{-10}	0.32	66.9	54.7	3.772	1.53	59.7	± 0.9
	2–6	3.584	8.614×10^{-10}	0.28	84.9	52.5	3.153	1.53	151.0	± 2.3
	6–10	2.946	8.798×10^{-10}	0.29	92.5	52.7	3.120	1.53	155.7	± 2.4

formation histories that are possibly very distant in time. Structural models aiming at describing the geometrical, mechanical, and potentially seismic evolution of faults should therefore at least attempt to account for the absolute timing of deformation responsible for the preserved fault architectures.

In a broader sense, this study confirms the complexity that likely characterizes many faults and helps to better conceptualize and plan the investigations needed to understand the broad spectrum of possible slip behaviours that faults may experience during their progressive deformation histories. In the case of the ZF, the identification and characterization of multiple BSFs as part of a time-constrained evolutionary scheme confirms the progressively narrowing character of the fault as it continued its episodic activity at progressively shallower crustal levels. From a more continuous deformation style in a brittle–ductile regime ca. 22 Ma ago forming the pervasively foliated phyllonitic domain of BSF 3, defined by anastomosing easy-glide, talc-defined planes embedding more competent calcareous lithons (e.g. Collettini et al., 2009) and foliated cataclasites and gouges, the fault system progressively embrittled, leading to foliated and massive cataclasites and finally to a discrete PSS at ca. < 5 Ma. During this ca. 18 Myr, a fluid-assisted evolution (Gundlach-Graham et al., 2018) can be reasonably coupled with a progressive temperature decrease during exhumation en route to the surface.

The documented complex spatial juxtaposition of BSFs highlights a remarkable geological heterogeneity within the ZF. Geological heterogeneity in fault zones has long been known to exist and, above all, to occur over a broad range of scales (e.g. Faulkner et al., 2003; Collettini et al., 2009; Fagereng et al., 2011; Tesei et al., 2014; Curzi et al., 2020a; Wang et al., 2016; Scheiber et al., 2019, and ref-

erences therein). Indeed, faults are commonly heterogeneous, anisotropic, and discontinuous in both along-strike and down-dip directions. This complexity is reflected by a broad spectrum of geometrical, mechanical, and hydrological properties at all scales, which is not always easy to resolve. Structural, mineralogical, and petrophysical heterogeneities in faults are being increasingly recognized as key players governing the mechanics of faulting (in addition to also affecting reservoir fluid compartmentalization, mineralization formation, etc.; Bruhn et al., 1990; Stober and Bucher, 2015; Scuderi et al., 2020; Bedford et al., 2022; Volpe et al., 2022) and thus attract much attention from the scientific community. The complexity and heterogeneity documented for the ZF are typical of long-lived, mature, and regional-scale fault systems (Viola et al., 2016; Aldega et al., 2019; Vignaroli et al., 2020). Their clear-cut characterization, however, is challenged by (i) coexisting multiple strands formed at different depths and (ii) the juxtaposition of BSFs resulting from different deformation conditions (Viola et al., 2013; Torgersen and Viola, 2014; Tartaglia et al., 2020). The net slip behaviour of faults (seismic vs. aseismic) is therefore the result of the interplay between local and regional stresses, combined with the varying environmental conditions and fault rock evolution.

We conclude by stressing that we are convinced that the illustrated workflow and the BSF approach may be pivotal to well-informed studies of faulting in space and through time and of the mechanical implications thereof.

6.3 The Zuccale Fault activity and implications of the new dates upon the tectonic evolution of the Northern Apennines

Lastly, we consider the implications that the new results have upon the reconstruction of the Miocene–Pliocene evolution of the Northern Apennines as recorded within the nappe stack of eastern Elba.

It is remarkable that no direct faulting ages have so far been reported for the Oligocene to early Miocene structuring stage of the eastern Elba nappe complex as part of the Northern Apennines orogenic wedge (e.g. Keller and Pialli, 1990; Vai and Martini, 2001), when nappe imbrication and regional northeast-vergent folding accommodated most of the regional shortening. Only recently, Curzi et al. (2020) reported a 22.1 Ma K–Ar age (statistically identical to the Aquitanian ages of our ZF samples) from a discrete thrust on the Island of Zannone in the Pontine Islands (central Italy) and interpreted it as representing the oldest available radiometric constraint on thrusting in the inner part of the central Apennines. By proposing a correlation between the siliciclastic turbidites in the footwall of the Zannone thrust and the Oligocene–Miocene Macigno Fm. farther to the north, Curzi et al. (2020) suggested Zannone to represent the southernmost exposed continuation of the Northern Apennines early Miocene (∼ 22 Ma) foredeep and thrust front, which was advancing toward the east and northeast in both the northern and central Apennines.

However, while the thrust dated to the early Miocene on Zannone has not been debated as to its kinematic significance, the ZF has in recent years become the target of an interesting scientific debate concerning its kinematic interpretation. As mentioned earlier, a very popular school of thought suggests the ZF to be a LANF, which would have accommodated a significant component of crustal extension in the late Miocene and the Pliocene within the geodynamic framework of the opening of the northern Tyrrhenian Sea back-arc basin (e.g. Keller and Pialli, 1990; Daniel and Jolivet, 1995; Collettini and Holdsworth, 2004). Alternatively, we advocate a second school of thought wherein the ZF is the brittle expression of faulting along the flat segment of an early Miocene–early Pliocene regional-scale thrust (Musumeci et al., 2015; Viola et al., 2018) that crosscuts older regional and local tectonic structures. According to this alternative model, the latest documented activity on the brittle ZF would have displaced the previously formed nappe stack by ca. 6 km to the east without any significant footwall exhumation or hanging wall block rotation, and thus is not a major player for a history of continuous extension in the area from the Miocene onward.

Samples ZUC 6 and ZUC 8 from this study are thus very important as they document, for the first time, Aquitanian top-to-east shearing along the ZF and therefore in the Northern Apennines. The data confirm the correlation proposed by Curzi et al. (2020) by directly documenting evidence of very early Miocene east-vergent tectonic transport

in the innermost part of the Northern Apennines. The earliest Miocene, when under-plating and deformation of the wedge were causing diffuse nappe stacking, is undoubtedly too early for extension in this sector of the Northern Apennines (e.g. Carmignani et al., 1995, and references therein). Only later, in the middle Miocene, would the uppermost part of the wedge be dismembered by remarkable low-angle extensional faulting causing thinning by tectonic elision of the nappe pile (e.g. Massa et al., 2017). A straightforward conclusion is therefore that within the ZF there occur Aquitanian BSFs that formed and isotopically equilibrated (for the investigated K–Ar system) at a time when nappes were still being shortened and imbricated in the growing orogenic wedge.

Viola et al. (2018) suggested a tectonic compressive event of Late Miocene–Pliocene age following the main phase of early Miocene nappe imbrication, as recorded by their samples ZUC 4 and ELB 2, dated to 6.14 ± 0.64 and 4.9 ± 0.27 Ma, respectively. Those two samples were taken from the Calanchiole Shear Zone and the CN–MAT, two inverse brittle–ductile to brittle faults in the immediate footwall of the ZF and directly cut across by it. Direct geometric field constraints from those deformation zones and the ZF allowed the authors to conclude that the last slip event recorded by the ZF postdates the youngest dated structure cut across by it in the footwall, i.e. the CN–MAT dated to 4.9 Ma. As mentioned above, modelling of a 7.58 Ma spurious age from sample ZUC 2 (Viola et al., 2018) by removing only ∼ 1 % of a contaminant of 300 Ma age contained within the Cretaceous Flysch at the expense of which the gouge of ZUC 2 formed (a reasonable assumption for a siliciclastic rock containing clasts from Paleozoic sources) brought the ZF faulting age to < 4.90 Ma (Viola et al., 2018). In a regional perspective, those late Miocene–early Pliocene ages and the kinematics of the dated structures confirm the existence of a deformation phase affecting the Oligocene to Miocene Northern Apennine wedge accommodating localized and relatively short-lived out-of-sequence thrusting (e.g. Boccaletti and Sani, 1998; Bonini et al., 2014).

The new K–Ar data presented here strengthen that inference, with ZUC 1 partially duplicating the results of sample ZUC 2 by Viola et al. (2018), and thus giving credit to a late slip phase along the ZF at < 4.9 Ma.

In summary, we conclude that an Aquitanian thrust (selectively preserved in some of the BSFs of the current ZF) was partially reactivated and exploited by the Pliocene ZF. During the ZF progressive deformation and fault reactivation, the Aquitanian BSFs underwent further transport and transposition and finally became juxtaposed against other BSFs, which formed later on within the core of the ZF, forming the current complex "patchwork" of fault rocks and K–Ar ages.

In the context of such long and articulated kinematic evolution, it is currently impossible to establish the origin of all BSFs and to constrain the amount of their finite transport within the progressively developing ZF core. Interestingly, preservation of Aquitanian dates within the finest size frac-

tions of samples ZUC 6 and ZUC 8 excludes significant thermal overprinting of the sampled BSFs by the LP–HT metamorphic overprint due to the late Miocene Porto Azzurro pluton. Indeed, the documented LP–HT thermal anomaly associated with the emplacement and cooling of the pluton (reaching up to 650 °C; e.g. Duranti et al., 1992; Caggianelli et al., 2018; Papeschi et al., 2019) would have reset the isotopic signature of the dated Aquitanian BSFs if they had been exposed to such high temperature for sufficiently long times. This consideration suggests transport and final juxtaposition of BSFs at their current location from root areas far away from the Porto Azzurro pluton, where they would have escaped any overprinting effects of the thermal anomaly. Moreover, the preserved Aquitanian age in BSF 1 strengthens the deduction that the Pliocene brittle ZF postdated the Porto Azzurro emplacement (i.e. Musumeci et al., 2015).

The considerations above, together with independent constraints on the tectonic history of the Northern Apennines, are summarized and used to propose the possible evolutionary model illustrated in Fig. 9, where we reconstruct the progressive tectonic evolution that we envisage for the ZF. Crustal shortening of Aquitanian age led to stacking of metamorphic units that experienced high pressure and low temperature (HP–LT) in the deep portion of orogenic wedge (Fig. 9a; Ryan et al., 2021, and references therein). A large-scale duplex of imbricated horses made of metamorphic units might be envisaged as being capped by a roof thrust that separates it from the overlying upper portion of wedge (Fig. 9a). The latter consisted of the sedimentary and/or very low-grade metamorphic sequences stacked in a nappe structure consisting of the Tuscan Nappe and the overlying Ligurian units. The ZF would have started to form at this stage, aiding shortening and nappe imbrication in the progressively growing wedge. In addition to our new ZF K–Ar ages documenting this stage, at the regional scale Oligocene–Aquitanian orogenic wedge shortening is also constrained by other lines of evidence, including (i) the K–Ar radiometric ages for the first deformation phase (D1) in the metamorphic units of the Apuane Alps, dated to ca. 27 Ma (Kligfield et al., 1986), (ii) the tectonic emplacement of Ligurian units above the Tuscan Nappe dated to the late Oligocene–Langhian (Montanari and Rossi, 1982), and (iii) the late Oligocene age of the Macigno Fm. sediment deposition (Dallan-Nardi, 1977). Moreover, late Oligocene ages of 25 and 27–30 Ma have been reported for HP–LT assemblages on the island of Gorgona and Monte Argentario, respectively (Brunet et al., 2000). Another 20.9 Ma Aquitanian Ar / Ar age has been recently reported for HP metamorphism and tectonic exhumation of the Acquadolce HP–LT unit in the metamorphic complex of eastern Elba (Ryan et al., 2021). The still quite loosely constrained age interval for HP–LT blueschist facies metamorphism recorded in several units of the Northern Apennines between 27 and 20 Ma, however, could indicate the diachronous development of subduction and exhumation of units in the deep orogenic wedge.

As shown in Fig. 9a, samples ZUC 6 and ZUC 8 may be regarded as representative of tectonic slices belonging to the roof thrust between the Upper Complex and Lower Complex in the orogenic wedge. Thus, the "old" Aquitanian ZF might correspond to a still-preserved segment of the original roof thrust that contributed to the tectonic extrusion dynamics of the deeply seated units within the wedge (e.g. Ryan et al., 2021).

After a widely acknowledged episode of mid-Miocene extension affecting the uppermost orogenic wedge that led to the formation of the highly tectonically excised "Serie Ridotta" of the Tuscan Nappe (Trevisan, 1950; Perrin, 1975; Decandia et al., 1993) in response to the wedge internal dynamics (i.e. gravitational re-equilibration of an overcritical wedge; e.g. Massa et al., 2017; Fig. 9b), a new shortening phase was recorded in the entire Northern Apennines orogenic wedge and affected both the already exhumed metamorphic units and the Tuscan Nappe and Ligurian units. This late Miocene–early Pliocene phase resulted from the activity of out-of-sequence thrusts ranging in age from Tortonian to early Pliocene. On eastern Elba, this is documented by (i) the Tortonian Rio Marina Thrust (Massa et al., 2017), (ii) the late Messinian Calanchiole and Felciaio shear zones (6.0 Ma; Musumeci and Vaselli 2012; Viola et al., 2018), and (iii) the CN–MAT (4.9 Ma; Viola et al., 2018; Fig. 9c).

During the late Miocene, the Porto Azzurro pluton was emplaced in this actively deforming area. Several scenarios contemplating different emplacement mechanisms have been proposed in the last few decades for the Porto Azzurro pluton. Its emplacement was originally attributed to space creation by extension accommodating local gravitational instabilities (e.g. Trevisan, 1950; Pertusati et al., 1993). Subsequently, the pluton emplacement was interpreted as being coeval with extensional regional faulting within the Northern Apennines upper crust (e.g. Smith et al., 2010) or with oblique, transtensional tectonics (Liotta et al., 2015). Recently, according to Spiess et al. (2021), the Porto Azzurro pluton has been interpreted as actually being a synkinematic intrusion emplaced in the footwall of the active Zuccale Fault. The results of geological mapping of the host Calamita Peninsula (Papeschi et al., 2017, 2021, 2022), along with meso- and micro-structural analysis of the host rock fabric (Mazzarini et al., 2011; Musumeci and Vaselli, 2012) and direct dating of deformation features cutting through the granite (Viola et al., 2018 and this study), however, suggest that the Porto Azzurro pluton emplaced into the Ortano and Calamita units during overall crustal shortening and certainly before the last recorded early Pliocene activity of the ZF (Musumeci et al., 2015; Viola et al., 2018). Figure 9d depicts the stage of early emplacement of the Porto Azzurro pluton within an overall compressive stage of the evolution of the wedge.

Finally, the entirely brittle, early Pliocene ZF (< 4.9 Ma, sample ZUC 1 and ZUC 2; Viola et al., 2018; this work, Fig. 9e) is interpretable as the youngest out-of-sequence
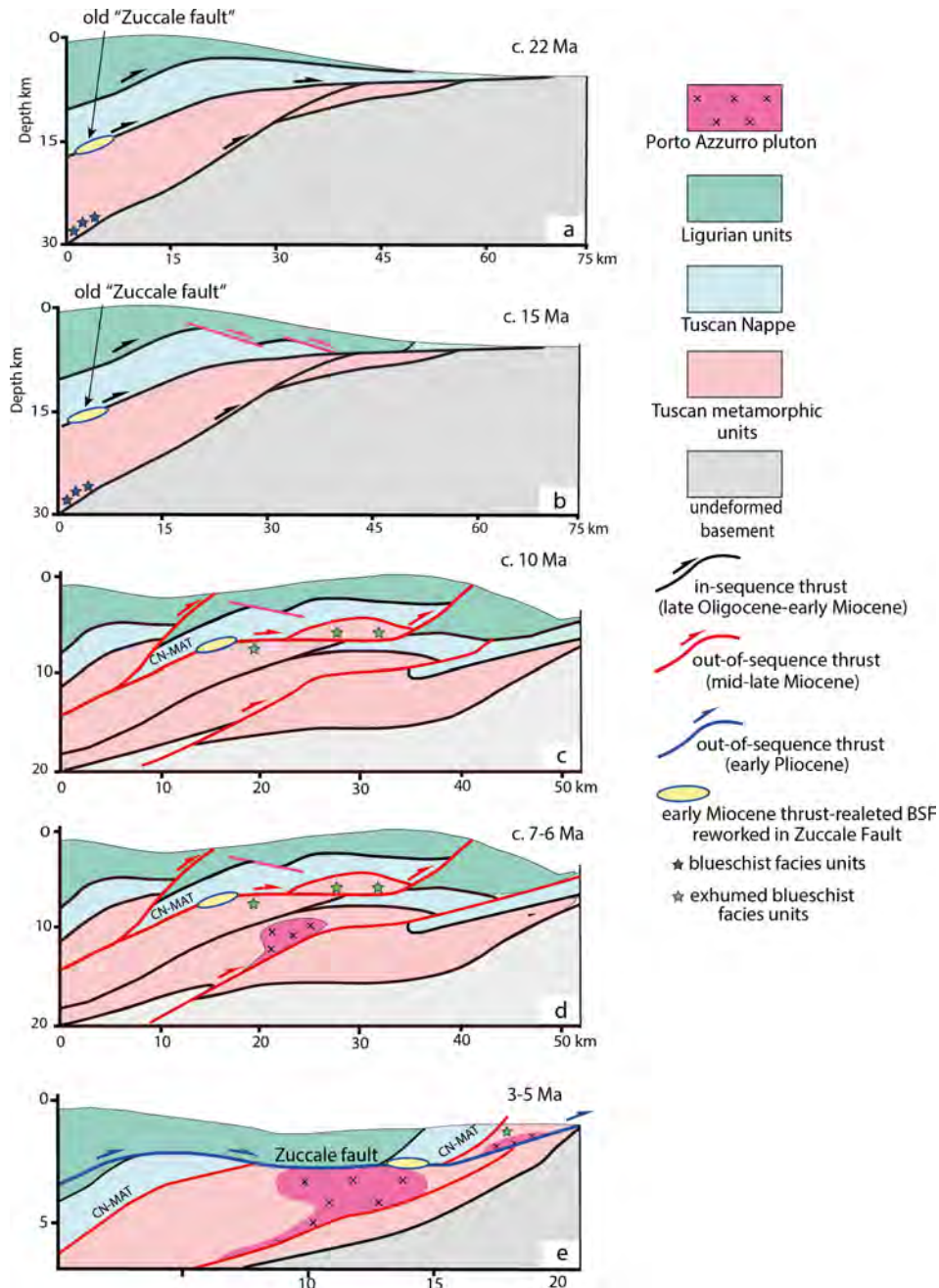
Figure 9. Diagram illustrating the envisaged tectonic evolution of the Northern Apennines belt for the early Miocene–early Pliocene time interval. Note the progressive zooming in to shallower crustal levels for panels **(c)**–**(e)** compared to **(a)** and **(b)**. Panel **(e)** zooms into panel **(d)** and describes a possible scenario for the late Miocene–early Pliocene. Note that, for simplicity sake, the diagrams do not depict the post-Pliocene and still-active extension. **(a)** Early Miocene nappe stacking with development of east-vergent in-sequence thrusts. Deep metamorphic units experienced HP–LT blueschist facies metamorphism (0.9–1.5 GPa). **(b)** In the mid-Miocene the uppermost wedge was affected by significant extension causing tectonic excision and thinning of the Ligurian units and of the Tuscan Nappe. **(c)** Late Miocene thrust reactivation and coeval development of east-vergent out-of-sequence thrusts that reshape the early Miocene nappe stack. Deep metamorphic units exhumed to greenschist facies conditions in the upper orogenic wedge are coupled with supra-crustal non-metamorphic to very low metamorphic grade units. **(d)** The Porto Azzurro pluton emplaced in the late Miocene in a contractional scenario similar to that of **(c)** (e.g. Mazzarini et al., 2011; Musumeci and Vaselli, 2012; Papeschi et al., 2017). **(e)** Early Pliocene evolution of central–eastern Elba. The out-of-sequence ZF cuts the nappe stack and Porto Azzurro pluton. Previous Tortonian out-of-sequence thrusts (e.g. the Capo Norsi–Monte Arco Thrust, CN–MAT) were reactivated, cut across, and displaced by the ZF in the early Pliocene (< 4.9 Ma). The architecture of the Northern Apennine belt on Elba was profoundly reshaped by the activity of multiple out-of-sequence thrusts spanning in age from late Miocene to early Pliocene.

thrust that decapitated the stack of tectonic units and the late Miocene intrusive rocks and their contact aureole (Calamita unit; Musumeci and Vaselli 2012; Papeschi et al., 2017).

As the last out-of-sequence structure that cut across the nappe stack, the brittle ZF partly sampled, reworked, and transposed previous structures that now are preserved as "host blocks" in the "cataclastic matrix" of the fault, thus contributing to the complex spatial juxtaposition of the described BSFs. The flat segment of the thrust now exposed in eastern Elba cuts across the late Miocene nappe stack with a kilometric horizontal displacement. This displacement notwithstanding, it preserves the same sequence of units in both the hanging wall and footwall (Fig. 9e), as clearly seen on geological maps and in the field. Late Miocene–Pliocene out-of-sequence thrusting in eastern Elba is additionally supported by recent geological mapping of the nappe stack of west-dipping tectonic units in easternmost Elba (Papeschi et al., 2021), wherein rocks affected by very low-grade regional metamorphism are thrusted over metamorphic units with late Miocene high-temperature metamorphism.

7   Conclusions

The combined structural and geochronological study of the ZF has allowed us to learn lessons of general validity that can be used to define suitable approaches to reconstruct the time-constrained structural and mechanical evolution of architecturally complex fault zones. Additionally, we have gained an in-depth and refined understanding of the complex evolution through time of the ZF, which is a major fault of the inner portion of the Northern Apennines that can be used to better constrain the Neogene evolution of the belt.

The main highlights of this work can be summarized as follows.

i. Brittle faults are unique archives of the stress state and physical and chemical conditions at the time of both initial deformation localization and subsequent slip(s). Progressive deformation may lead to complex fault architectures, the unravelling of which is at times challenging because, once formed, faults are extremely sensitive to variations in stress field and are prone to readily slip in a variety of environmental conditions. The detailed, multi-scalar structural analysis of faults and of fault rocks has thus to be the starting point for any study aiming at reconstructing the complex framework of brittle deformation. However, considering that present-day exposures of faults only represent the end result of often protracted and heterogeneous histories, structural and mechanical results need to be integrated over the lifespan of the studied fault system. K–Ar gouge dating to constrain the time-integrated evolution of faults is therefore the natural addition to detailed structural studies. The brittle structural facies concept by Tartaglia et al. (2020) effectively combines these approaches, allowing the high-resolution reconstruction of brittle deformation histories and, in turn, multiple constraints to be placed on deformation localization, deformation mechanisms, fluid flow, mineral alteration and authigenesis within actively deforming brittle fault rocks.

ii. The BSF approach has revealed that the ZF is architecturally complex and composed of at least six different BSFs. K–Ar gouge dating has constrained an unexpectedly long faulting activity spanning a ca. 20 Myr time interval in the framework of the evolution of the Northern Apennines. We envisage a scenario wherein the ZF started as an Aquitanian thrust that was then selectively reactivated by early Pliocene out-of-sequence thrusts during the progressive structuring of the Northern Apennine wedge. The current fault architecture is a heterogeneous patchwork of BSFs formed at very different times under different P–T conditions in a top-to-the-east kinematic framework.

iii. The structural framework of the Northern Apennines can be elegantly accounted for by a model of continuous convergence between the late Oligocene and the early Pliocene with a major intervening phase of extension in the mid-Miocene allowing for the isostatic re-equilibration of the wedge. Extension started again in the Pliocene and is still active in the innermost portion of the Northern Apennines.

Author contributions. GV conceptualized the study, did fieldwork, acquired the data, collected the samples, elaborated the data, wrote the original draft of the manuscript, and prepared the figures. GM and FM did fieldwork, acquired the data, elaborated the data, wrote part of the text, and prepared a few of the figures. LT mapped the BSFs during his master thesis. MC did fieldwork, helped with conceptualization and data interpretation, and assisted with preparing a few of the figures. ET conceptualized the study, did fieldwork, collected the samples, and contributed to text review and editing. RvdL dated the samples and performed TEM imaging. LA ran the XRD analyses and contributed to text review, editing, and discussions.

References

Aldega, L., Viola, G., Casas-Sainz, A., Marcén, M., Román-Berdiel, T., and Lelij, R.: Unravelling multiple thermo-tectonic events accommodated by crustal-scale faults in northern Iberia, Spain: Insights from K-Ar dating of clay gouges, Tectonics, 38, 3629–3651, https://doi.org/10.1029/2019tc005585, 2019.

Barberi, F., Innocenti, F., and Ricci, C. A.: Il complesso scistoso di Capo Calamita (Isola d'Elba), Atti Della Società Toscana Di Scienze Naturali Residente a Pisa, Memorie Ser. A, 72, 579–617, 1967.

Barboni, M., Annen, C., and Schoene, B.: Evaluating the construction and evolution of upper crustal magma reservoirs with coupled U / Pb zircon geochronology and thermal modeling: A case study from the Mt. Capanne pluton (Elba, Italy), Earth Planet. Sc. Lett., 432, 436–448, https://doi.org/10.1016/j.epsl.2015.09.043, 2015.

Bedford, J. D., Faulkner, D. R., and Lapusta, N.: Fault rock heterogeneity can produce fault weakness and reduce fault stability, Nat. Commun., 13, 326, https://doi.org/10.1038/s41467-022-27998-2, 2022.

Bianco, C., Brogi, A., Caggianelli, A., Giorgetti, G., Liotta, D., and Meccheri, M.: HP-LT metamorphism in Elba Island: Implications for the geodynamic evolution of the inner Northern Apennines (Italy), J. Geodyn., 91, 13–25, https://doi.org/10.1016/j.jog.2015.08.001, 2015.

Boccaletti, M. and Sani, F.: Cover thrust reactivations related to internal basement involvement during Neogene-Quaternary evolution of the northern Apennines, Tectonics, 17, 112–130, https://doi.org/10.1029/97tc02067, 1998.

Boccaletti, M., Elter, P., and Guazzone, R.: Plate tectonics models for the development of Western Alps and northern Apennines, Nature, 234, 108–111, 1971.

Bonini, M., Sani, F., Stucchi, E. M., Moratti, G., Benvenuti, M., Menanno, G., and Tanini, C.: Late Miocene shortening of the Northern Apennines back-arc, J. Geodyn., 74, 1–31, https://doi.org/10.1016/j.jog.2013.11.002, 2014.

Bortolotti, V., Fazzuoli, M., Pandeli, E., Principi, G., Babbini, A., and Corti, S.: Geology of Central and Eastern Elba Island, Italy, Ofioliti, 26, 97–150, 2001.

Braathen, A., Tveranger, J., Fossen, H., Skar, T., Cardozo, N., Semshaug, S. E., Bastesen, E., and Sverdrup, E.: Fault facies and its application to sandstone reservoirs, AAPG Bull., 93, 891–917, https://doi.org/10.1306/03230908116, 2009.

Bruhn, R. L., Yonkee, W. A., and Parry, W. T.: Structural and Fluid-Chemical Properties of Seismogenic Normal Faults, Tectonophysics, 175, 139–157, https://doi.org/10.1016/0040-1951(90)90135-U, 1990.

Brunet, C., Monié, P., Jolivet, L., and Cadet, J.-P.: Migration of compression and extension in the Tyrrhenian Sea, insights from $^{40}Ar / ^{39}Ar$ ages on micas along a transect from Corsica to Tuscany, Tectonophysics, 321, 127–155, 2000.

Caggianelli, A., Zucchi, M., Bianco, C., Brogi, A., and Liotta, D.: Estimating P-T metamorphic conditions of the roof of a hidden granitic pluton: an example from the Mt. Calamita promontory (Elba Island, Italy), Ital. J. Geosci., 137, 238–253, https://doi.org/10.3301/IJG.2018.11, 2018.

Caine, J. S., Evans, J. P., and Forster, C. B.: Fault zone architecture and permeability structure, Geology, 24, 1025–1028, 1996.

Carboni, F., Viola, G., Aldega, L., Van Der Lelij, R., Brozzetti, F., and Barchi, M. R.: K-Ar fault gouge dating of Neogene thrusting: the case of the siliciclastic deposits of the Trasimeno Tectonic Wedge (Northern Apennines, Italy), Ital. J. Geosci., 139, 1–13, https://doi.org/10.3301/ijg.2020.06, 2020.

Carmignani, L., Decandia, F. A., Disperati, L., Fantozzi, P. L., Lazzarotto, A., Liotta, D., and Oggiano, G.: Relationships between the Tertiary structural evolution of the Sardinia-Corsica-Pronencal Domain and the Northern Apennines, Terra Nova, 7, 128–137, 1995.

Carmignani, L., Decandia, F. A., Disperati, L., Fantozzi, P. L., Kligfield, R., Lazzarotto, A., Liotta, D., and Meccheri, M.: Inner northern Apennine, in: Anatomy of an orogen: The Apennines and adjacent Mediderranean basins, edited by: Vai, G. B. and Martini, I. P., 197–214, Springer-Science + Business Media, B.V., ISBN 978-90-481-4020-6, https://doi.org/10.1007/978-94-015-9829-3, 2001.

Collettini, C.: The mechanical paradox of low-angle normal faults: Current understanding and open questions, Tectonophysics, 510, 253–268, https://doi.org/10.1016/j.tecto.2011.07.015, 2011.

Collettini, C. and Holdsworth, R. E.: Fault zone weakening and character of slip along low-angle normal faults: insights from the Zuccale fault, Elba, Italy, J. Geol. Soc., 161, 1039–1051, https://doi.org/10.1144/0016-764903-179, 2004.

Collettini, C., Viti, C., Smith, S. A. F., and Holdsworth, R. E.: Development of interconnected talc networks and weakening of continental low-angle normal faults, Geology, 37, 567–570, https://doi.org/10.1130/g25645a.1, 2009.

Collettini, C., Niemeijer, A., Viti, C., Smith, S. A. F., and Marone, C.: Fault structure, frictional properties and mixed-mode fault slip behavior, Earth Planet. Sc. Lett., 311, 316–327, https://doi.org/10.1016/j.epsl.2011.09.020, 2011.

Curzi, M., Aldega, L., Bernasconi, S. M., Berra, F., Billi, A., Boschi, C., Franchini, S., Van der Lelij, R., Viola, G., and Carminati, E.: Architecture and evolution of an extensionally-inverted thrust (Mt. Tancia Thrust, Central Apennines): Geological, structural, geochemical, and K–Ar geochronological constraints, J. Struct. Geol., 104059, https://doi.org/10.1016/j.jsg.2020.104059, 2020a.

Curzi, M., Billi, A., Carminati, E., Rossetti, F., Albert, R., Aldega, L., Cardello, G. L., Conti, A., Gerdes, A., Smeraglia, L., Van der Lelij, R., Vignaroli, G., and Viola, G.: Disproving the Presence of Paleozoic-Triassic Metamorphic Rocks on the Island of Zannone (Central Italy): Implications for the Early Stages of the Tyrrhenian-Apennines Tectonic Evolution, Tectonics, 39, e2020TC006296, https://doi.org/10.1029/2020tc006296, 2020b.

Dallan-Nardi, L.: Segnalazione di Lepidocydine nella parte basale dello "pseudomacigno" delle Alpi Apuane, B. Soc. Geol. Ital., 95, 459–477, 1977.

Daniel, J. M. and Jolivet, L.: Detachment faults and pluton emplacement; Elba Island (Tyrrhenian Sea), B. Soc. Géol. France, 166, 341–354, https://doi.org/10.2113/gssgfbull.166.4.341, 1995.

Decandia, F. A., Lazzarotto, A., and Liotta, D.: La "serie ridotta" nel quadro dell'evoluzione geologica della Toscana meridionale, Memorie Soc. Geol. Ital., 49, 181–191, 1993.

Dini, A., Innocenti, F., Rocchi, S., Tonarini, S., and Westerman, D. S.: The magmatic evolution of the late Miocene laccolith–pluton–dyke granitic complex of Elba Island, Italy, Geol. Mag., 139, 257–279, 2002.

Duranti, S., Palmeri, R., Pertusati, P. C., and Ricci, C. A.: Geological evolution and metamorphic petrology of the basal sequences of eastern Elba (Complex II), Acta Vulcanologica, 2, Marinelli Volume, 213–229, 1992.

Eberl, D. D., Środoń, J., Lee, M., Nadeau, P. H., and Northrup, H. R.: Sericite from the Silverton caldera, Colorado: Correlation among structure, composition, origin, and particle thickness, Am. Mineral., 72, 914–934, 1987.

Faccenna, C., Becker, T. W., Miller, M. S., Serpelloni, E., and Willett, S. D.: Isostasy, dynamic topography, and the elevation of the Apennines of Italy, Earth Planet. Sc. Lett., 407, 163–174, https://doi.org/10.1016/j.epsl.2014.09.027, 2014.

Fagereng, Å., Remitti, F., and Sibson, R. H.: Incrementally developed slickenfibers – Geological record of repeating low stress-drop seismic events?, Tectonophysics, 510, 381–386, https://doi.org/10.1016/j.tecto.2011.08.015, 2011.

Faulkner, D. R., Lewis, A. C., and Rutter, E. H.: On the internal structure and mechanics of large strike-slip fault zones: field observations of the Carboneras fault in southeastern Spain, Tectonophysics, 367, 235–251, https://doi.org/10.1016/s0040-1951(03)00134-3, 2003.

Gagnevin, D., Daly, J. S., Horstwood, M. S. A., and Whitehouse, M. J.: In-situ zircon U–Pb, oxygen and hafnium isotopic evidence for magma mixing and mantle metasomatism in the Tuscan Magmatic Province, Italy, Earth Planet. Sc. Lett., 305, 45–56, https://doi.org/10.1016/j.epsl.2011.02.039, 2011.

Gundlach-Graham, A., Garofalo, P. S., Schwarz, G., Redi, D., and Günther, D.: High-resolution, Quantitative Element Imaging of an Upper Crust, Low-angle Cataclasite (Zuccale Fault, Northern Apennines) by Laser Ablation ICP Time-of-Flight Mass Spectrometry, Geostand. Geoanal. Res., 42, 559–574, https://doi.org/10.1111/ggr.12233, 2018.

Hałas, S. and Wójtowicz, A.: Propagation of error formulas for K/Ar dating method, Geochronometria, 41, 202–206, 2014.

Hunziker, J. C., Frey, M., Clauer, N., Dallmeyer, R. D., Friedrichsen, H., Flehmig, W., Hochstrasser, K., Roggwiler, P., and Schwander, H.: The evolution of illite to muscovite: mineralogical and isotopic data from the Glarus Alps, Switzerland, Contrib.

Mineral. Petr., 92, 157–180, https://doi.org/10.1007/bf00375291, 1986.

Keller, J. V. A. and Coward, M. P.: The structure and evolution of the northern Tyrrhenian Sea, Geol. Mag., 103, 1–16, 1996.

Keller, J. V. A. and Pialli, G.: Tectonics of the Island of Elba: A reappraisal, B. Soc. Geol. Ital., 109, 413–425, 1990.

Kligfield, R., Hunziker, J. C., Dallmeyer, R. D., and Schamel, S.: Dating deformation phases using K-Ar and $^{40}A/^{39}Ar$ techniques: results from the Northern Apennines, J. Struct. Geol., 8, 781–786, 1986.

Lee, J. Y., Marti, K., Severinghaus, J. P., Kawamura, K., Yoo, H. S., Lee, J. B., and Kim, J. S.: A redetermination of the isotopic abundances of atmospheric Ar, Geochim. Cosmochim. Ac., 70, 4507–4512, 2006.

Liotta, D., Brogi, A., Meccheri, M., Dini, A., BIanco, C., and Ruggieri, G.: Coexistence of low-angle normal and high-angle strike- to oblique-slip faults during Late Miocene mineralization in eastern Elba Island (Italy), Tectonophysics, 660, 17–34, https://doi.org/10.1016/j.tecto.2015.06.025, 2015.

Lippolt, H. J., Wernicke, R. S., and Baehr, R.: Paragenetic specularite and adularia (Elba, Italy): Concordand (U + Th)-He and K-Ar ages, Earth Planet. Sc. Lett., 132, 43–51, 1995.

Mancktelow, N., Zwingmann, H., Campani, M., Fugenschuh, B., and Mulch, A.: Timing and conditions of brittle faulting on the Silltal-Brenner Fault Zone, Eastern Alps (Austria), Swiss J. Geosci., 108, 305–326, https://doi.org/10.1007/s00015-015-0179-y, 2015.

Massa, G., Musumeci, G., Mazzarini, F., and Pieruccioni, D.: Coexistence of contractional and extensional tectonics during the northern Apennines orogeny: the late Miocene out-of-sequence thrust in the Elba Island nappe stack, Geol. J., 52, 353–368, https://doi.org/10.1002/gj.2761, 2017.

Mazzarini, F., Musumeci, G., and Cruden, A. R.: Vein development during folding in the upper brittle crust: The case of tourmaline-rich veins of eastern Elba Island, northern Tyrrhenian Sea, Italy, J. Struct.Geol., 33, 1509–1522, https://doi.org/10.1016/j.jsg.2011.07.001, 2011.

McDougall, I. and Wellman, P.: Calibration of GA1550 biotite standard for K / Ar and $^{40}Ar/^{39}Ar$ dating, Chem. Geol., 280, 19–25, 2011.

Montanari, L. and Rossi, M.: Evoluzione delle Uniti stratigrafico – strutturali del Nord Appennino: 1 – L'Unità di Canetolo, B. Soc. Geol. Ital., 101, 275–289, 1982.

Moore, D. M. and Reynolds, R. C. J.: X-ray diffraction and the identification and analysis of clay minerals, Oxford University Press, Oxford, 378 pp., ISBN 9780195087130, 1997.

Musumeci, G. and Vaselli, L.: Neogene deformation and granite emplacement in the metamorphic units of northern Apennines (Italy): Insights from mylonitic marbles in the Porto Azzurro pluton contact aureole (Elba Island), Geosphere, 8, 470–490, https://doi.org/10.1130/Ges00665.1, 2012.

Musumeci, G., Mazzarini, F., and Cruden, A. R.: The Zuccale Fault, Elba Island, Italy: A new perspective from fault architecture, Tectonics, 34, 1195–1218, https://doi.org/10.1002/2014tc003809, 2015.

Papeschi, S. and Musumeci, G.: Fluid assisted strain localization in quartz at the brittle/ductile transition, Geochem. Geophy. Geosy., 20, 3044–3064, https://doi.org/10.1029/2019gc008270, 2019.

Papeschi, S., Musumeci, G., and Mazzarini, F.: Heterogeneous brittle-ductile deformation at shallow crustal levels under high thermal conditions: The case of a synkinematic contact aureole in the inner northern Apennines, southeastern Elba Island, Italy, Tectonophysics, 717, 547–564, https://doi.org/10.1016/j.tecto.2017.08.020, 2017.

Papeschi, S., Musumeci, G., Massonne, H. J., Bartoli, O., and Cesare, B.: Partial melting and strain localization in metapelites at very low-pressure conditions: The northern Apennines magmatic arc on the Island of Elba, Italy, Lithos, 350/351, 105230, https://doi.org/10.1016/j.lithos.2019.105230, 2019.

Papeschi, S., Musumeci, G., Massonne, H. J., Mazzarini, F., Ryan, E. J., and Viola, G.: High-P (P = 1.5–1.8 GPa) blueschist from Elba: Implications for underthrusting and exhumation of continental units in the Northern Apennines, J. Metamor. Geol., 38, 495–525, https://doi.org/10.1111/jmg.12530, 2020.

Papeschi, S., Ryan, E., Musumeci, G., Mazzarini, F., Garofalo, P. S., and Viola, G.: Geology of the Northern Apennines nappe stack on eastern Elba (Italy): new insights on the Neogene orogenic evolution of the Northern Tyrrhenian Sea, J. Maps, 17, 519–532, https://doi.org/10.1080/17445647.2021.1972854, 2021.

Perrin, M.: L'Ile d'Elbe et la limite Alpes-Apennin: données sur la structure géologique et l'evolution tectogénétique de l'Elbe alpine et de l'Elbe apennine, B. Soc. Geol. Ital., 94, 1929–1955, 1975.

Pertusati, P. C., G., R., Ricci, C. A., Duranti, S., and Palmeri, R.: Evoluzione post-collisionale dell'Elba centtro-orientale, Mem. Soc. Geol. It, 49, 297–312, 1993.

Pevear, D. R.: Illite and hydrocarbon exploration, P. Natl. Acad. Sci. USA, 96, 3440–3446, 1999.

Renne, P. R., Deino, A. L., Hames, W. E., Heizler, M. T., Hemming, S. R., Hodges, K. V., Koppers, A. A. P., Mark, D. F., Morgan, L. E., and Phillips, D.: Data reporting norms for 40Ar/39Ar geochronology, Quat. Geochronol., 4, 346–352, https://doi.org/10.1016/j.quageo.2009.06.005, 2009.

Ryan, E., Papeschi, S., Viola, G., Musumeci, G., Mazzarini, F., Torgersen, E., Sørensen, B. E., and Ganerød, M.: Syn-orogenic exhumation of high-P units by upward extrusion in an accretionary wedge: Insights from the Eastern Elba nappe stack (Northern Apennines, Italy), Tectonics, 40, e2020TC006348, https://doi.org/10.1029/2020tc006348, 2021.

Scheiber, T., Viola, G., van der Lelij, R., Margreth, A., and Schönenberger, J.: Microstructurally-constrained versus bulk fault gouge K-Ar dating, J. Struct. Geol., 127, 103868, https://doi.org/10.1016/j.jsg.2019.103868, 2019.

Schumacher, E.: Herstellung von 99, 9997 % ^{38}Ar für die ^{40}K / ^{40}Ar Geochronologie, Geochronologia Chimia, 24, 441–442, 1975.

Scuderi, M. M., Tinti, E., Cocco, M., and Collettini, C.: The Role of Shear Fabric in Controlling Breakdown Processes During Laboratory Slow-Slip Events, J. Geophys. Res.-Sol. Ear., 125, e2020JB020405, https://doi.org/10.1029/2020jb020405, 2020.

Sibson, R. H.: Fault rocks and fault mechanisms, J. Geol. Soc., 133, 191–213, https://doi.org/10.1144/gsjgs.133.3.0191, 1977.

Smith, S. A. F. and Faulkner, D. R.: Laboratory measurements of the frictional properties of the Zuccale low-angle normal fault, Elba Island, Italy, J. Geophys. Res., 115, B02407, https://doi.org/10.1029/2008jb006274, 2010.

Smith, S. A. F., Holdsworth, R. E., and Collettini, C.: Interactions between low-angle normal faults and plutonism in the upper crust: Insights from the Island of Elba, Italy, Geol. Soc. Am. Bull., 123, 329–346, https://doi.org/10.1130/b30200.1, 2011a.

Smith, S. A. F., Holdsworth, R. E., Collettini, C., and Pearce, M. A.: The microstructural character and mechanical significance of fault rocks associated with a continental low-angle normal fault: The Zuccale Fault, Elba Island, Italy, in: Geological Society of London Special Publication: Geology of the Earthquake Source: A Volume in Honour of Rick Sibson, edited by: Fagereng, Å., Toy, V. G., and Rawland, J. V., Geol. Soc. Lond., 359, 97–113, https://doi.org/10.1144/SP359.6, 2011b.

Spiess, R., Langone, A., Caggianelli, A., Stuart, F. M., Zucchi, M., Bianco, C., Brogi, A., and Liotta, D.: Unveiling ductile deformation during fast exhumation of a granitic pluton in a transfer zone, J. Struct. Geol., 147, 104326, https://doi.org/10.1016/j.jsg.2021.104326, 2021.

Steiger, R. and Jäger, E.: Subcommission on geochronology: convention on the use of decay constants in geo-and cosmochronology, Earth Planet. Sc. Lett., 36, 359–362, 1977.

Stober, I. and Bucher, K.: Hydraulic conductivity of fractured upper crust: insights from hydraulic tests in boreholes and fluid-rock interaction in crystalline basement rocks, Geofluids, 15, 161–178, https://doi.org/10.1111/gfl.12104, 2015.

Tartaglia, G., Viola, G., van der Lelij, R., Scheiber, T., Ceccato, A., and Schönenberger, J.: "Brittle structural facies" analysis: A diagnostic method to unravel and date multiple slip events of long-lived faults, Earth Planet. Sc. Lett., 545, 116420, https://doi.org/10.1016/j.epsl.2020.116420, 2020.

Tesei, T., Collettini, C., Barchi, M. R., Carpenter, B. M., and Di Stefano, G.: Heterogeneous strength and fault zone complexity of carbonate-bearing thrusts with possible implications for seismicity, Earth Planet. Sc. Lett., 408, 307–318, https://doi.org/10.1016/j.epsl.2014.10.021, 2014.

Torgersen, E. and Viola, G.: Structural and temporal evolution of a reactivated brittle-ductile fault – Part I: Fault architecture, strain localization mechanisms and deformation history, Earth Planet. Sc. Lett., 407, 205–220, https://doi.org/10.1016/j.epsl.2014.09.019, 2014.

Torgersen, E., Viola, G., Zwingmann, H., and Harris, C.: Structural and temporal evolution of a reactivated brittle-ductile fault – Part II: Timing of fault initiation and reactivation by K-Ar dating of synkinematic illite/muscovite, Earth Planet. Sc. Lett., 410, 212–224, https://doi.org/10.1016/j.epsl.2014.11.013, 2015a.

Torgersen, E., Viola, G., Zwingmann, H., and Henderson, I. H. C.: Inclined K-Ar illite age spectra in brittle fault gouges: effects of fault reactivation and wall-rock contamination, Terra Nova, 27, 106–113, https://doi.org/10.1111/ter.12136, 2015b.

Trevisan, L.: L'Elba orientale e la sua tettonica di scivolamento per gravità, Memorie Istituto Geologia Università Padova, 16, 5–39, 1950.

Vai, G. B. and Martini, I. P. (Eds.): Anatomy of an Orogen: The Apennines and Adjacent Mediterranean Basins, 637 pp., Springer-Science + Business Media, B.V., ISBN 978-90-481-4020-6, https://doi.org/10.1007/978-94-015-9829-3, 2001.

Vignaroli, G., Viola, G., Diamanti, R., Zuccari, C., Garofalo, P. S., Bonini, S., and Selli, L.: Multistage strain localisation and fluid-assisted cataclasis in carbonate rocks during the seismic cycle: Insights from the Belluno Thrust (east-

ern Southern Alps, Italy), J. Struct. Geol., 141, 104216, https://doi.org/10.1016/j.jsg.2020.104216, 2020.

Viola, G., Zwingmann, H., Mattila, J., and Kapyaho, A.: K-Ar illite age constraints on the Proterozoic formation and reactivation history of a brittle fault in Fennoscandia, Terra Nova, 25, 236–244, https://doi.org/10.1111/ter.12031, 2013.

Viola, G., Scheiber, T., Fredin, O., Zwingmann, H., Margreth, A., and Knies, J. M.: Deconvoluting complex structural histories archived in brittle fault zones, Nat. Commun., 7, 13448, https://doi.org/10.1038/ncomms13448, 2016.

Viola, G., Torgersen, E., Mazzarini, F., Musumeci, G., van der Lelij, R., Schönenberger, J., and Garofalo, P. S.: New Constraints on the Evolution of the Inner Northern Apennines by K-Ar Dating of Late Miocene-Early Pliocene Compression on the Island of Elba, Italy, Tectonics, 37, 3229–3243, https://doi.org/10.1029/2018tc005182, 2018.

Volpe, G., Pozzi, G., Carminati, E., Barchi, M. R., Scuderi, M. M., Tinti, E., Aldega, L., Marone, C., and Collettini, C.: Frictional controls on the seismogenic zone: Insights from the Apenninic basement, Central Italy, Earth Planet. Sci. Lett., 583, 117444, https://doi.org/10.1016/j.epsl.2022.117444, 2022.

Wang, Y., Zwingmann, H., Zhou, L. Y., Lo, C. H., Viola, G., and Hao, J. H.: Direct dating of folding events by Ar^{40}/Ar^{39} analysis of synkinematic muscovite from flexural-slip planes, J. Struct. Geol., 83, 46–59, https://doi.org/10.1016/j.jsg.2015.12.003, 2016.

Westerman, D. S., Dini, A., Innocenti, F., and Rocchi, S.: Rise and fall of a nested Christmas-tree laccolith complex, Elba Island, Italy, in: Physical Geology of High-Level Magmatic Systems, edited by: Breitkreuz, C. and Petford, N., Geol. Soc. Lond., 234, 195–213, 2004.

Wibberley, C. A. J. and Shimamoto, T.: Internal structure and permeability of major strike-slip fault zones: the Median Tectonic Line in Mie Prefecture, Southwest Japan, J. Struct. Geol., 25, 59–78, https://doi.org/10.1016/S0191-8141(02)00014-7, 2003.

Wise, D. U., Dunn, D. E., Engelder, J. T., Geiser, P. A., Hatcher, R.D., Kish, S. A., Odom, A. L., and Schamel, S.: Fault-related rocks: Suggestions for terminology, Geology, 12, 391–394, https://doi.org/10.1130/0091-7613(1984)12<391:FRSFT>2.0.CO;2, 1984.